Science Arts & Métiers (SAM)

To cite this version :

Multiscale study of additively manufactured 316 L microstructure sensitivity to heat treatment over a wide temperature range

Hugo Roirand [a, b, c], Alessandro Pugliara [a, d], Benoit Malard [a], Anis Hor [b, *], Nicolas Saintier [c]

[a] CIRIMAT, Université de Toulouse, INPT, CNRS, UPS, 4 Allée Emile Monso, 31030 Toulouse, France
[b] ICA, Université de Toulouse, CNRS, ISAE-SUPAERO, 3 rue Caroline Aigle, 31400 Toulouse, France
[c] I2M, Arts et métiers ParisTech, CNRS, Esplanade des arts et métiers, 33400 Talence, France
[d] Centre de Micro-Caractérisation Raimond Castaing, Université de Toulouse, UPS, CNRS, INPT, INSA, 3 rue Caroline Aigle, 31400 Toulouse, France

ABSTRACT

Keywords:
Heat treatment
Additive manufacturing
Sigma phase
Nano-oxides
Dislocation

The main subject of this study is to investigate the correlations between the evolution of mechanical behavior and the multiscale microstructure of 316 L stainless steel obtained by laser powder bed fusion process (LPBF) after various post-manufacturing heat treatments across a wide temperature range. The microstructure of 316 L LPBF parts exhibits a hierarchical microstructure based on unique grain structures, chemical segregations, dislocation arrangements at the microscopic scale and fine nano-oxides at the nanoscopic scale. These microstructural elements play a crucial role in determining the material's mechanical and corrosion properties. To understand how different microstructural features contribute to the material's behavior, the researchers conduct post-manufacturing heat treatments to isolate and study these components. The results show that dislocation and/or micro-segregation networks significantly influence the high tensile properties of 316 L LPBF steel in its as-built state and after heat treatments above 900°C. Despite their disappearance during heat treatments, the material maintains high tensile strength due to an increase in strain-hardening capabilities. The study also examines the impact of nano-oxides and the σ phase on the material's properties. The contribution of nano-oxides to yield strength diminishes with increasing temperature. Interestingly, the σ phase does not necessarily lead to a detrimental effect on failure elongation for 316 L LPBF steel. Overall, this research provides insights into the relationship between microstructure and mechanical properties for additively manufactured stainless steel. By understanding these relationships, it becomes possible to tailor the microstructure to achieve desired mechanical properties for specific applications and extend the use of 316 L LPBF to higher temperatures compared to conventional methods.

1. Introduction

Stainless steels have good mechanical strength and corrosion behavior, notably compared to their relatively low cost. For these reasons they have been widely used for many years, especially in agri-food [1] and nuclear industries [2]. With the recent rise of additive manufacturing (AM) processes, there is renewed interest in these materials. The opportunities raised by AM processes are very numerous: topological optimization, lattices structures, microstructure tailoring, etc. As a result of these new possibilities, stainless steels are processed by AM in order to repair existing pieces, to create new complex geometries or to reduce the waste of raw materials in machining operations [3]. However, even though wrought stainless-steel alloys are well known, their AM counterparts differ in many aspects such as surface finish, residual stresses and microstructure. As a result, they have different mechanical and chemical properties. For instance, Racot et al. [4] have shown that the breakdown potential in 4 mol.l-1 of NaCl at 50°C is approximately 0.6 V for 316 L laser powder bed fusion (LPBF) compared to 0.1 V for conventional 316 L. Furthermore, Bahl et al. [5] showed that mechanical properties, and more specifically, the yield strength and the elongation at rupture are often much higher for AM 316 L than for conventional 316 L. These high mechanical and corrosion properties are due to the particular microstructure of 316 L LPBF parts. Thanks to AM processes, new grain structures, which were not accessible with conventional processes, can be achieved: Highly textured materials [6], specimens with tortuous grains [5] or crystallographic lamellar

microstructures [7]. In addition, at the microscopic scale, 316 L LPBF is composed of fine nano-oxides, chemical segregations, and dislocation arrangements in the as-built (AB) state [8]. This multiscale microstructure plays a key role in mechanical behavior [9,10] and corrosion properties [11]. Moreover, it can be controlled with AM parameters [12] or by using heat treatments [13]. The multiscale control of the microstructure is an opportunity to select microstructural features in relation with the intended properties. However, especially for mechanical properties, contributions of each microstructural features to the macroscopic properties have to be estimated. This is of the aim of this paper.

To study this, post-manufacturing heat treatments (PMHT) are key means for isolating microstructural components and understand their strengthening effect. Riabov et al. used PMHT to demonstrate the strengthening effect of the dislocation cells resulting from the LPBF process [14]. However, only three different PMHT temperatures were studied, rendering the analysis of the evolution of mechanical properties insufficient. Moreover, in most studies the evolution of microsegregation and dislocation cells is not covered separately, involving a very large temperature range of cell disappearance (See Table 1 in [13]). This paper will help to clarify and understand these discrepancies by separating the micro-segregation cells and the dislocation cells evolutions.

On the other hand, Chao et al. studied in greater detail the effect of PMHT on mechanical properties [15]. This study underlines the precipitation of embrittling sigma phase at grain boundaries for PMHT at 800°C for 2 h. Conversely, Voisin et al. [13], Sprouster et al. [11] and Lei et al. [16] failed to identify this type of precipitation or drop in elongation at rupture. Moreover, Kurzynowski et al. [17] found sigma phase after PMHT without noticing significant reduction in elongation at rupture. Consequently, the precipitation of sigma phase and its effect on mechanical properties need to be investigated in order to clarify these discrepancies.

At a finner scale, nano-oxides are dispersed in LPBF stainless steels [18–20]. A new interest for this microstructural feature has recently emerged with the idea to build net-shaped oxide dispersion strengthened (ODS) alloys with the LPBF process. Indeed, some authors argue that nano-oxides help to strengthen the 316 L [10,18,19], as for ODS steels [21], although Wang et al. [9] have estimated their contribution to be negligible. Such contrary results would be explained as the nano-oxides strengthening effect is highly dependent of their size [21]. Moreover, their size distribution also significantly modify corrosion resistance [22,23] and impact toughness [20,24]. It has been already demonstrated that nano-oxides size is sensitive to PMHT [20]. However, work is needed to correlate the nano-oxides coarsening to their strengthening contribution after different PMHTs.

Consequently, this paper proposes to correlate the evolution of mechanical behavior with the multiscale microstructure after numerous PMHTs over a wide temperature range (500°C-1200°C). This work is necessary to be able, in the future, to tailor the microstructure of 316 L LPBF to achieve the mechanical properties targeted for specific applications. In addition, this work is motivated by the objective of extending the use of 316 L LPBF to higher temperatures than for conventional counterparts.

2. Materials and methods

2.1. Powders and sample building

Samples were fabricated on an SLM125HL machine with powders provided by Höganäs with the composition detailed in Table 1. Fig. 1 illustrates the good sphericity of this powder (necessary property in LPBF) with granulometry in line with the recommendations of the machine supplier (15–45 μm powders).

Cylinders with a height of 96 mm and a diameter of 13 mm were manufactured under argon flux, with a pre-heating of the baseplate to 100°C, and the LPBF parameters recommended by SLM for 316 L stainless steel (Table 2).

The baseplate used in this study was full of vertical samples (45 samples, dimension of baseplate: 125 mm × 125 mm) and so, the building time was approximately 48 h. The chessboard laser scan strategy with islands containing 20 scan vectors (2.4 mm × 2.4 mm) was used. A 67° rotation of the pattern was applied between the layers.

2.2. Heat treatments

PMHT were conducted under secondary vacuum on AB samples. The AB state correspond to the material after manufacturing and before any heat treatment. The furnace used is a secondary vacuum furnace which allows to realize heat treatments in a controlled atmosphere. It is equipped with a cold shelter and a sliding carriage facilitating the insertion of samples into the high-temperature zone once the desired temperature is attained, all while maintaining the furnace's vacuum integrity without necessitating its opening.

Initially, samples were situated within the cold enclosure on the sliding carriage. Then, a primary vacuum was established to evacuate most of the air within the entire furnace. It is then filled with argon until a pressure of 1 atm was reached, followed by the attainment of both primary and secondary vacuum conditions. This procedure removes most of the oxygen molecules.

Samples were introduced into the high-temperature region once the desired temperature was achieved, maintaining a vacuum level below 5.10^{-5} mbar. The PMHT was conducted for a duration of 2 h at the
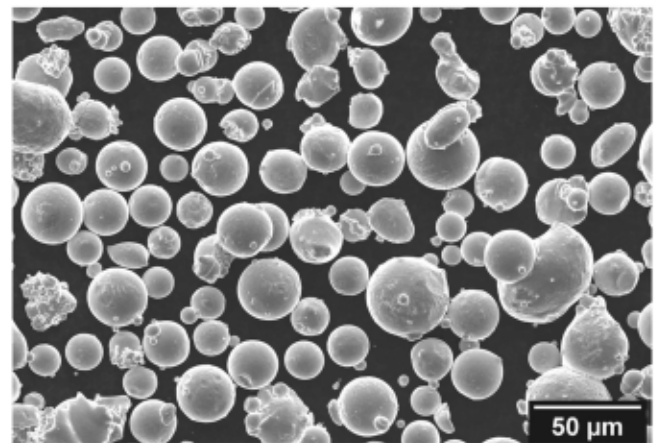

Fig. 1. SEM image of powders.

Table 1
Alloyed elements (*in weighted*%) of powder compared to EN-10028-7 standard [25]. Fe is the principal element. *O content (resp. N content) has been measured by chemical dosage at 352 ppm (resp. 105 ppm).

Element	Cr	Ni	Mo	Mn	Si	O	N	P	C	S
Powder	17.7	13.6	2.7	1.5	<0.1	0.04*	0.01*	<0.01	<0.01	0.002
EN-10028-7	16.5–18.5	10.0–13.0	2.0–2.5	≤2.0	≤1.0	<0.1	≤0.1	≤0.045	≤0.03	≤0.015

Table 2

LPBF process parameters. P is the laser power, v_l the laser velocity, t the layer thickness, h the hatch distance and D the laser spot diameter.

P (W)	v_l (mm/ s)	t (Åμm)	h (Åμm)	D (Åμm)	Scan strategy	Layers rotation
275	700	50	120	70–75	Chessboard	67°

prescribed temperature, after which the furnace was gradually cooled under vacuum conditions until the ambient temperature in the high-temperature region was reached. It is noteworthy that all characterization samples and tensile specimens underwent identical heat treatment procedures, displaying no discernible signs of oxidation subsequent to the heat treatments.

2.3. Characterization methods

2.3.1. Microstructure characterization by optical and scanning electron microscopy

For microstructural characterization by scanning electron microscopy (SEM) and optical microscopy (OM), samples were polished with the following sequence of SiC paper: P400, P600, P1200, P2400, P4000; then polished with 3 μm and 1 μm diamond suspensions and finally with an OPS solution. To reveal grain boundaries, micro-segregation cells and intergranular precipitates, samples were etched with aqua regia (HNO3 + HCl) for 1 min.

A Zeiss Axiovert A1m OM and a Leo 435 VP SEM were used for the microstructural characterizations. Energy dispersive X-ray spectroscopy (EDS) analysis and electron backscatter diffraction (EBSD) mapping were performed with a JEOL 7100F SEM. The step size for EBSD measurement for the AB specimen has been set to 0.5 μm and the step size for the PMHT specimen at 1200°C to 1.2 μm. EBSD data were cleaned and analyzed using Atex software [26]. Spikes correction (tolerance angle of 1.0° and minimum 7 neighbours) and zero solution correction (tolerance angle of 1.0° and minimum 7 neighbours, full correction up to 4 neighbours) have been used to cleaned the raw data.

From EBSD measurements, the average intra-granular disorientation has been calculated. Based on De Sonis et al. [27] paper, a grain is considered as recrystallized when its mean intragranular desorientation (θ_{mean})is below 1°. Surface fraction of recristallized grains is then:

$$f_{RX} = \frac{S_{\theta_{mean}<1°}}{S_{tot}} \tag{1}$$

with $S_{\theta_{mean}<1°}$ the grain surface for which $\theta_{mean} < 1°$, and S_{tot} the total analyzed surface. However, AB grains may show intragranular desorientations below 1° without being recrystallized. Then, the recrystallized ratio is defined as:

$$f_{RX}^{real} = \frac{f_{RX} - f_{RX}^{AB}}{1 - f_{RX}^{AB}} \tag{2}$$

avec f_{RX}^{AB} grain ratio for which $\theta_{mean} < 1°$ at the AB state. This surface fraction is calculated around 4% in De Sonis et al. paper [27].

2.3.2. Microstructure characterization by transmission electron microscopy

In order to perform transmission electron microscopy (TEM) observations, thin foils were cut with a wire saw, then mechanically polished to a thickness of 50–100 μm. After polishing, 2.2 mm squares were extracted from the thin foils. These were electro-polished using a solution containing 95% methanol and 5% perchloric acid in a TENUPOL-5 system under 14 V at −25°C. Analyses were carried out using a JEOL-2100F TEM operated at 200 kV equipped with an EDS analyser (Brucker SDD XFlash 5030) and a STEM detector. Diffraction patterns were recorded using selected area electron diffraction (SAED) mode with a 150 nm aperture or a digital diffraction pattern obtained by fast Fourier transform (FFT) of high-resolution TEM (HRTEM) images. All

diffraction patterns were indexed using the diffraction pattern simulation obtained with the CaRIne Crystallography program [28].

Concerning the measurement of dislocation cell diameter, diameter measurements were performed in several areas of each sample. Indeed, since the dislocation cells follow the solidification dendrites, the observation plane of these cells affects the observable diameter.

2.3.3. Analysis of dislocation densities

X-ray diffraction (XRD) measurements for dislocation density characterization were performed with a D8 Bruker Discover diffractometer equipped with a copper source. In order to deconvolute the signal due to instrumental configuration and physical parameters (microstrain and crystallite size), measurements were performed on an LaB_6 standard powder from the national Institute of Standards and technology (NIST). This LaB_6 powder is intended to have no microstrains and large crystallite size.

Measurements on 316 L LPBF stainless steel were then carried out with θ-θ mounting, with 2θ in the 20–120° range, with 0.05° step and 8 s of acquisition per point. The 316 L LPBF stainless steel samples are 2 mm high and 12 mm diameter cylinders. These were polished on one side (with normal parallel to building direction (BD)) using the sequence previously mentioned. Data were analyzed using Topas software to achieve the Rietveld method [29] and calculate the lattice parameter for each PMHT temperature. Then the Williamson and Hall method [30], was followed for microstrain and crystallite size determination. Based on these measurements, the dislocation densities ρ were calculated using the equation proposed by Williamson and Smallman as described in Mote et al. [31]:

$$\rho = \frac{2\sqrt{3}\,\varepsilon}{Db} \tag{3}$$

where D corresponds to the crystallite size (nm), ε represents the microstrains (%), and b is the Burgers vectors (nm). $b = a/\sqrt{2}$ for FCC structure with a the lattice parameter.

2.3.4. Tensile tests

An electromechanical Instron 5900R (100kN) testing system was used to perform tensile tests. Tensile specimen geometry is given in Fig. 2. Tensile specimens are machined from the cylinders built with the LPBF process (diameter = 13 mm, height = 96 mm). Heat treatments are realized after the machining in order to relief probable residual stresses induced by machining.

Tensile tests were performed along the BD (= vertical). Axial strain measurements were performed using an AVE2 Axial Instron video extensometer and tensile tests were carried at a strain rate of $8,3.10^{-5}$ s^{-1} until 0.5% of total strain, then $1,6.10^{-3}$ s^{-1} until fracture (according to NF EN 2002–001 standard). At least three tensile tests were performed for each PMHT.

3. Assumptions regarding microstructural contributor to alloy strengthening

The main goal of this paper is to correlate microstructural evolutions to tensile properties. It is focused on the relative contribution of microstructural features compared to the AB state. Therefore, contributions of the microstructural features which do not evolve through PMHT are not estimated. The main assumptions for strengthening contribution evaluation are summarized in the following paragraphs.

3.1. At microscopic scale

3.1.1. Dislocations

Dislocation cells are known to contribute strongly to the hardening mechanisms of 316 L LPBF steel. In particular, cell walls are obstacles to dislocation movement [8]. There are two methods for assessing their
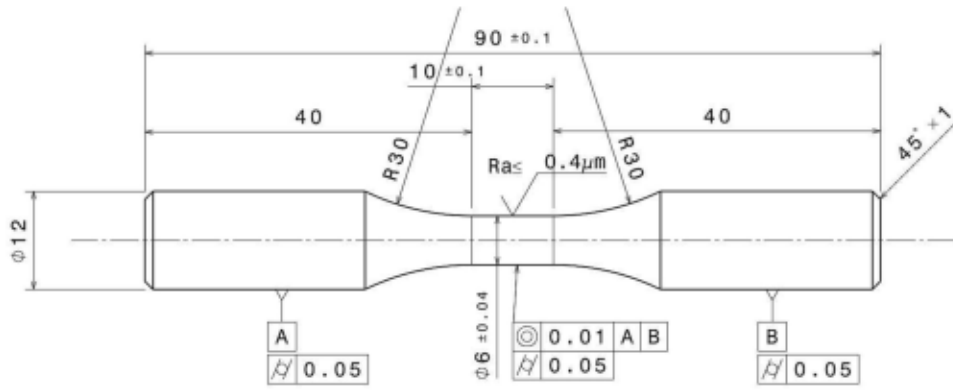
Fig. 2. Tensile specimen geometry.

contribution:

- By a Hall-Petch law [32], considering cell walls as grain boundaries [9,33]. However, this approach has recently been criticized on the grounds that the cells are weakly disoriented with respect to each other (< 0.5–$1°$ [34]) whereas the Hall-Petch law assumes strongly disoriented grain boundaries ($>15°$). Furthermore, counter-examples show that equivalent yield strengths can be obtained for significantly different cell sizes [34].
- By a Taylor law [35], based on the material's dislocation density. This is the approach adopted in this paper.

The following Taylor's law is therefore used to evaluate the contribution of dislocations to alloy strengthening:

$$\sigma_{Taylor} = M\alpha Gb\sqrt{\rho} \tag{4}$$

with M the Taylor factor (3.06 for fcc structures [36]), α an experimental constant (0.23, [37]), G the shear modulus (75 GPa, calculated from tensile test results, assuming isotropic behavior), b the Burger vector (nm). b is calculated from the experimental lattice parameter a, which is estimated from X-Ray measurements. $b = a/\sqrt{2}$ for fcc structures. ρ is the dislocation density (m^{-2}), estimated from X-Ray measurements.

3.1.2. Micro-segregations

There is no analytical formula for estimating the contribution of micro-segregations cells independantly of dislocation cells. Moreover, separating the contribution of both lattices seems very tricky, since interactions between the two lattices are likely to exist [34]. It is therefore hypothesized that the contribution of the micro-segregation network is included in that calculated for the dislocation network.

3.1.3. Sigma precipitates

When observed, σ precipitates are located at the grain boundaries. However, as the deformation mechanisms of 316 L LPBF steel are predominantly intragranular slip, the intergranular sigma phase is unlikely to be involved in alloy strengthening. Moreover, the size of σ phase precipitates is in the micrometer range, so their contribution to alloy hardening by bypass mechanisms would be insignificant. The contribution of the σ phase to hardening will therefore not be assessed.

3.2. Nanoscopic scale

3.2.1. Nano-oxides

In first assumption, only the average size of precipitates is used to calculate their contribution to alloy hardening. As nano-oxides are larger than few nanometers and very probably incoherent with matrix, Friedel shear mechanism [38] is not considered. On the contrary, Orowan bypass mechanism [38] is most suitable for such precipitates,

therefore Orowan's law is used to calculate the contribution of nano-oxides to the alloy hardening of 316 L LPBF steel:

$$\sigma_{Orowan} = \frac{Gb}{L} \quad with \quad L = R\sqrt{\frac{2\pi}{3f_p}} \tag{5}$$

with G the shear modulus of the matrix, b the Burgers vector, L the distance between particles. L is calculated assuming an homogeneous distribution of nano-oxides in the material, with f_p corresponding to the fraction of precipitates and R to their mean radius. This hypothesis of homogeneous distribution is supported by TEM observations (see Results).

4. Results and discussion

4.1. As-built microstructure

The AB microstructure has been characterized from the polycrystalline scale to the nanoscopic one in order to serve as the reference state from PMHT microstructures presented later (Fig. 3). No tremendous novelty has been reported compared to the literature dedicated to the microstructure of 316 L LPBF at the AB state.

4.1.1. Polycrystalline scale: melt pools, phases and grains

Figure 3a show the melt-pools inherent of the LPBF process. Melt pools contain several grains, however, grains are not restricted to one meltpool. Fig. 3b illustrates the AB microstructure observed by EBSD. It consists of elongated $\langle 100 \rangle$ austenitic grains along the BD, confirming the epitaxial growth throughout the layers as observed in Fig. 3a and as reported in the literature for 316 L LPBF [6,34,39]. It can be noted that some grains have a tortuous shape, which is caused by the epitaxial growth through layers combined with rotations of $67°$ between each layer. This is a direct consequence of side-branching growth as explained by Pham et al. [40]. Additionally, grains – especially large ones – show internal disorientations in the AB state, as shown by colour distribution in the grains. These are indicators of intragranular strain [41]. The XRD scans presented in Fig. 3c confirms the only presence of the face-centred cubic (FCC) austenitic phase as expected for this alloy [18,42].

4.1.2. Microscopic scale: micro-segregations and dislocations networks

Within the grains, micro-segregations following a cell pattern were revealed after etching and SEM observation (Fig. 3d). These micro-segregations are common in LPBF materials in the AB state [8]. Their formation is related to high cooling rates and is well described in Kong et al. [8] or in Dépinoy et al. [34]. For 316 L LPBF, they are enriched in Mo and Cr as revealed by Dépinoy et al. [43] and Bertsch et al. [44] thanks to STEM/EDS analysis. Micro-segregation cells are observed uniformly on all samples, however, because etching is sensitive to grain orientation, dislocation density, or local chemical composition, it does
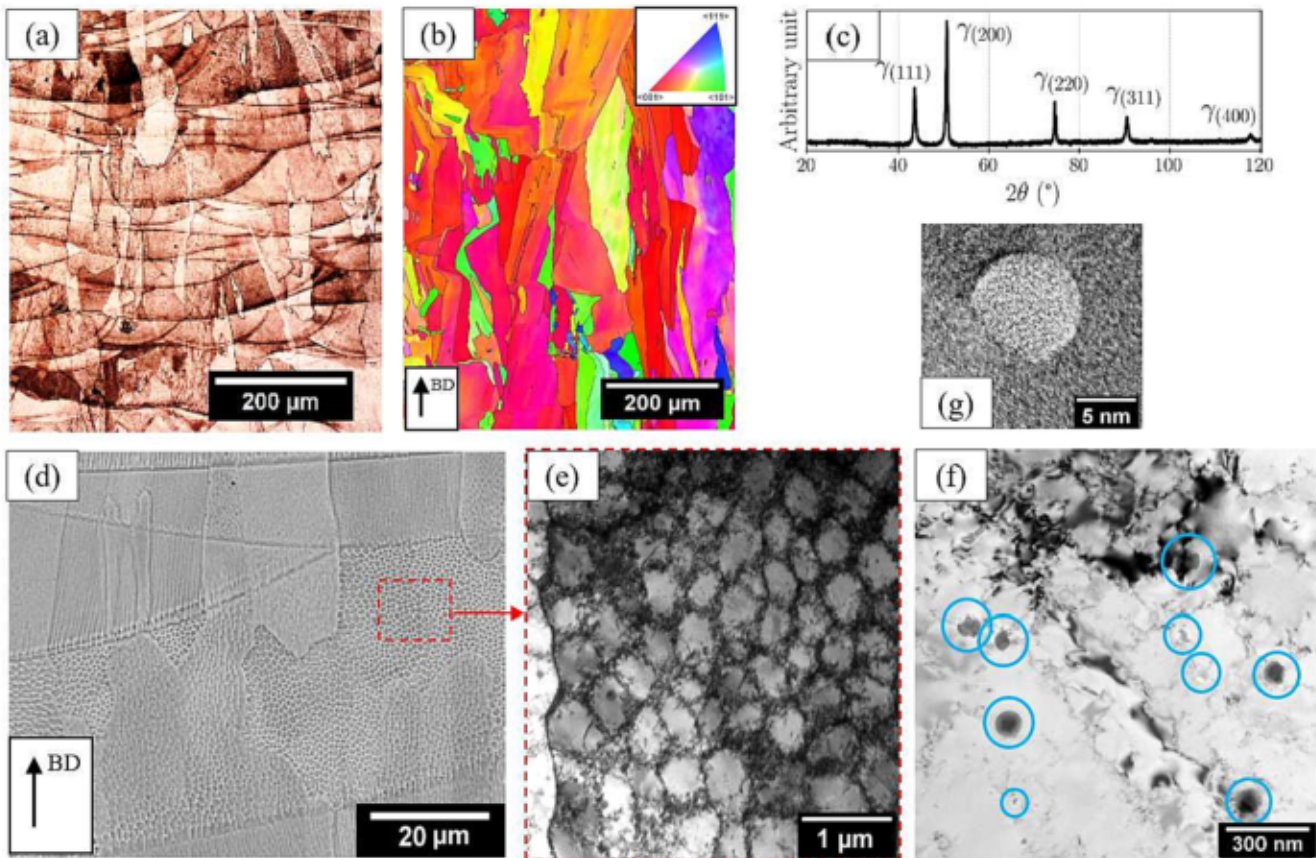
Fig. 3. Multiscale characterization of 316 L LPBF AB microstructure. (a) OM image revealing meltpools after etching. (b) EBSD inverse pole figure map showing grains. (c) X-Ray diffractogram revealing the unique austenitic phase. (d) Micro-segregation cells observed in SEM after etching. (e) Dislocation cell network revealed in TEM. (f) Nano-oxides observed in TEM, they are circled in blue for more visibility. (g) Zoom on one small nano-oxide with a crystalline structure. (For interpretation of the references to colour in this figure legend, the reader is referred to the web version of this article.)

not react in the same way everywhere and results in variations in the visibility of micro-segregations. At the AB state, the average diameter of micro-segregation cells has been estimated at 0.38 ± 0.08 μm.

As expected, TEM observations confirm the presence of dislocations organized in a 2D-network of cells (Fig. 3e); which correspond to dendrites in 3D. A relatively high density of dislocations is highlighted on cell boundaries, whereas cell interiors are almost free of dislocations. It is now accepted that dislocations are generated by thermal strains due to expansion/shrinkage after solidification in the LPBF process [34,44,45]. Based on the literature, dislocation dendrites fit with micro-segregation dendrites [8]. Dislocation cell diameter measurements are in accordance with this result. Indeed, the average diameter of dislocation cells observed in TEM has been calculated at 0.42 ± 0.04 μm which fits with the average micro-segregation cell size measured in SEM.

4.1.3. Nanoscopic scale: nano-oxides

At a finer scale, nano-oxides enriched in *Mn* and *Si* have been identified at the AB state (Fig. 3f,g). They show a spherical shape with a mean diameter calculated at 17 ± 2 nm and have a rhodonite crystalline structure which correlates with the observations of $MnSiO_3$ nano-oxides at the AB state by Yan et al. [19].

Precipitates are randomly distributed with respect to other microstructural characteristics, as reported by [46], but contrary to what has been observed by Voisin et al. [13].

4.2. Heat treatment influences at the polycrystalline scale

4.2.1. Meltpools stability

The laser tracks (or meltpool boundaries) are visible after etching in

OM at the AB state because of chemical heterogeneities between their center and boundaries [17]. The stability of the laser tracks was studied in order to obtain information on the activation temperatures of chemical solid diffusion during PMHTs. This information will help to interpret microstructure changes at lower scales.

As Fig. 4 shows, laser tracks are stable for PMHT at 650°C, they are less defined for PMHT at 800°C but still clearly visible. They disappear for PMHT between 800°C and 1000°C. These images express a start of diffusion process on long range scale ($\gtrsim 50 \mu m$) from 800°C. These processes generate a chemical homogenization at the polycrystalline scale for PMHT above 800°C. This hypothesis of thermally activated diffusion mechanisms is also supported by Ronneberg et al. [47].

4.2.2. Grain boundaries stability

Contrary to laser tracks, grains boundaries do not show any evolution for 2-h PMHTs from 500 to 1200°C as shown in Fig. 5. Indeed, these SEM images after etching show grain sizes, morphologies, and arrangements that are comparable between the different images and close to those of the AB state (see 3b).

Therefore, no recrystallization is observed even after a 2-h PMHT at 1200°C. In order to confirm this observation, EBSD analyses were performed on samples after PMHT at 1200°C (Fig. 5d).

Figure 5d reveals that the orientations of the PMHT material are close to those of the AB state (majority of grains <100>//BD). Moreover, internal disorientations remain visible within the grains. Finally, no twin boundaries can be observed in the sample analyzed. Yet recrystallization processes are known to suppress the majority of internal disorientations and are accompanied by twinning for 316 L LPBF steel [27,48]. The three observations cited above therefore run counter
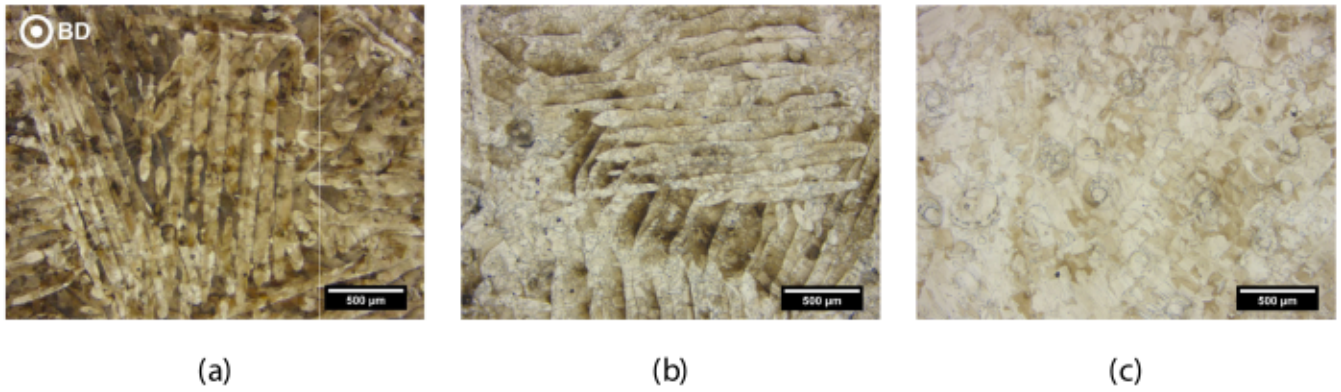
Fig. 4. OM images after etching for samples PMHT at (a) 650 °C, (b) 800 °C and (c) 1000 °C.
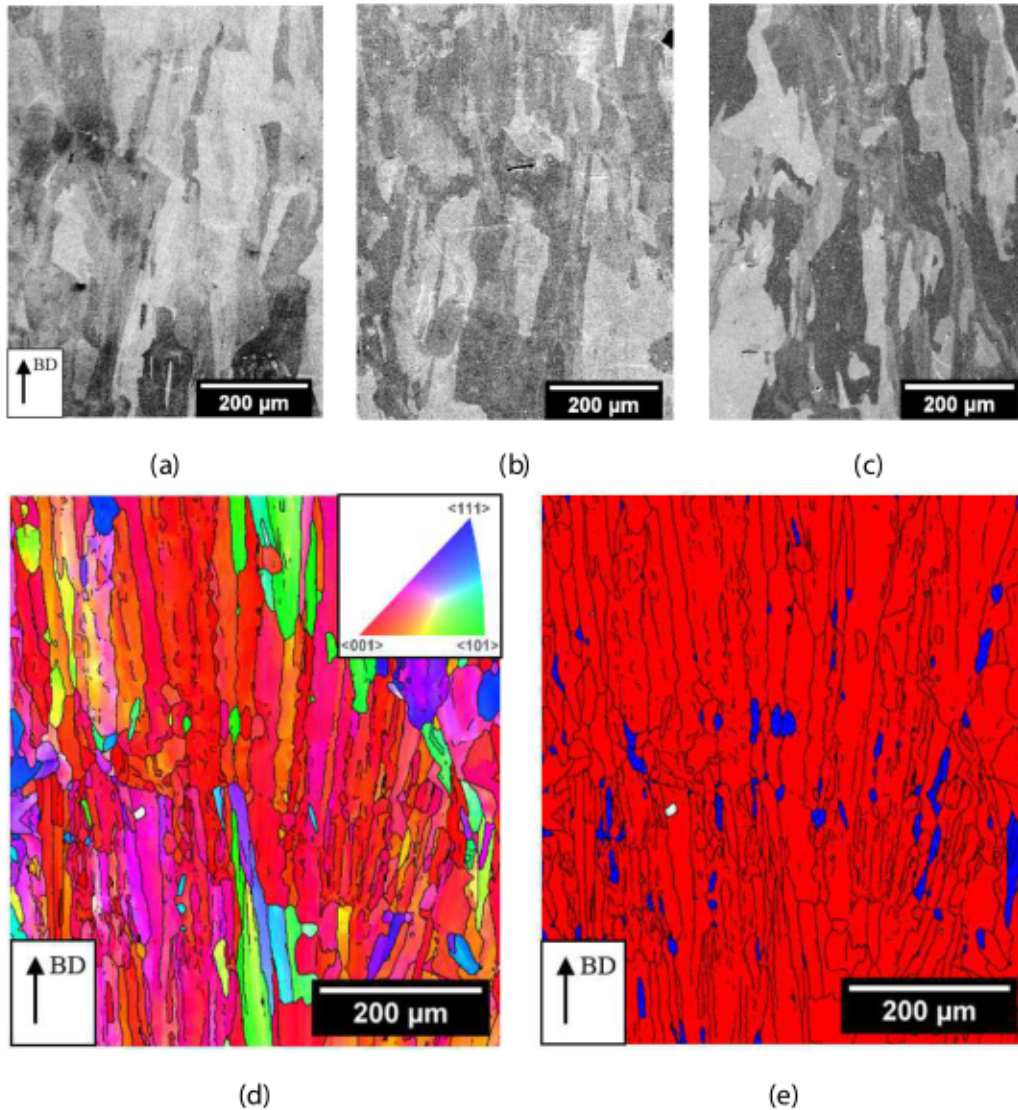

Fig. 5. SEM images after etching showing the polycrystalline microstructure for samples PMHT at (a) 650 °C, (b) 800 °C and (c) 1200 °C. (d) EBSD mapping of a sample PMHT at 1200 °C. In (e), the grains are colored according to their average intragranular disorientation $\theta_{average}$. For $\theta_{average} < 1°$, they are blue, otherwise red. (For interpretation of the references to colour in this figure legend, the reader is referred to the web version of this article.)

to a hypothesis supporting recrystallization.

To quantify this absence of recrystallization, the internal grain disorientation map was plotted in Fig. 5e. On this map, grains with an average internal disorientation $\theta_{average} > 1°$ are colored red, otherwise

blue. The fraction of grains with $\theta_{moy} < 1°$ is 3.8%, whereas it was measured at 4.3% in the AB condition. Consequently, the real fraction of recrystallized grains f_{RX}^{vraie}, defined in the methods' section 2, is equal to

zero. Based on these EBSD measurements of internal disorientations, the absence of recrystallization for the PMHT sample during 2 h at 1200°C is confirmed.

In the literature, Salman et al. [48] observed the onset of grain coarsening as early as 1000 °C and complete recrystallization at 1400 °C. Kong et al. [8], showed that grain boundaries are stable up to and including 1050°C, but that recrystallization occurs for PMHTs at 1200 °C. Tascioglu et al. [49] reported the onset of recrystallization for PMHTs at 1100 °C. Finally, De Sonis et al. [27] recently highlighted significant differences in recrystallization temperature (1100°C vs 1200°C) for two 316 L LPBF stainless steels built with same process parameters.

Differences in recrystallization temperature therefore exist between several studies in the literature and our own. Three main hypotheses could explain these differences:

- To begin, the PMHT method employed in this study distinguishes itself from the prevailing approaches found in existing literature. Specifically, in this investigation, samples are introduced into the preheated region of the furnace once it has reached the prescribed temperature, and subsequently held for a duration of two hours. Conversely, conventional practice in many laboratories and industrial settings involves the placement of samples within the furnace while it remains at ambient temperature. The temperature is then incrementally raised until it attains the desired level, at which point the dwell time is initiated. Consequently, this alternate methodology results in extended exposure of the samples to intermediate and elevated temperatures. This divergence in approach may elucidate the absence of recrystallization phenomena observed within our study following a two-hour PMHT at 1200°C, in contrast to the prevalent findings in the existing literature.
- Differences in low angle boundaries (LAB) density would explain discrepancies about recrystallization kinetics. This is the hypothesis advanced by De Sonis et al. [27] to explain their observations. They argue that LABs would increase the energy difference between grains at both sides of a high angle boundary, which would help to nucleate recrystallized grains by the strain induced boundary migration mechanism. Then, low LAB parts would have lower recrystallization kinetics. However, by following the methodology presented in their paper, the LAB density has been estimated at the AB state for our alloy at $9,1.10^4 \, m/m^2$ which is higher than for their alloy ($3,5.10^4 \, m/m^2$) which recrystallizes at 1200°C. Thus, the LAB density parameter is not sufficient to explain recrystallization temperature differences.
- Differences in chemical composition of powders could modify nano-oxide distributions and then affect recrystallization kinetics. Indeed, Voisin et al. [13] have compiled the chemical compositions of various powders and 316 L steel parts obtained in LPBF. They showed a wide dispersion in composition. For example, the mass percentage of Cr can vary by >4%, and that of Mn from 0.2 to 2% between different studies. Such wide variations in chemical composition inevitably have an impact on microstructural properties. For example, the number and nature of nano-oxides are affected by the oxygen content of the steel [50]. These nano-oxides slow down the movement of grain boundaries through mechanisms such as *Zenner-pinning* [19] and could reduce recrystallization kinetic as supported by [51].

Finally, none of hypothesis is fully convenient, further investigations would be required. However, this is not in the scope of this paper which aims more at investigating the impact of multiscale microstructure on mechanical behavior.

Nevertheless, 316 L LPBF polycrystalline microstructure is more stable and shows higher recrystallization temperature than conventional counterparts [13,27,51,52]. This could help at extend the use of 316 L LPBF alloys at higher temperature than for conventional 316 L.

4.3. Microscale evolution of the microstructure with heat treatment temperature

4.3.1. Chemical evolution of microstructure with heat treatment temperature

Figure 6 shows the evolution of micro-segregation cells and associated precipitates. Micro-segregation cells are present on samples from the AB state up to PMHT of around 700 °C. In some areas of samples treated at 750 and 800 °C, traces of cells remain. No cells were observed in samples treated at 900 °C and above. Thus, a gradual disappearance of micro-segregation cells takes place over a temperature range from 700 to 850°C. These observations are in good agreement with what is observed in the literature and reported by Voisin et al. [13].

This disappearance is associated with diffusion processes of the elements making up the cell walls (alphagene elements, mainly Cr, Mo, Si [8]). It is interesting to note that this temperature range (700–850°C) is lower than that associated with the disappearance of laser tracks observed in OM (800–1000°C) in Fig. 4. This is simply due to a scale factor effect: melt pools have characteristic widths of the order of a hundred microns, whereas cells have diameters less than one micron. As a result, chemical homogenization on the meltpools scale requires higher temperatures (at isoduration of treatment) to enable diffusion over a greater distance.

The disappearance of micro-segregation cells is immediately followed by coarse precipitation on the grain boundaries, as can be seen in Fig. 6c and d. These precipitates are first isolated (at triple grains boundaries), then as temperature increases, they grow and decorate the entire grain boundaries. They disappear between 1000°C and 1200°C as shown by Fig. 6e. These precipitates have been observed at multiple locations, on different samples after the same PMHT. Moreover, their presence has been also confirmed on the same temperature ranges for specimens built with the meander strategy and used for tensile tests.

The chemical composition of these precipitates was analyzed by EDS in the SEM, they are enriched in Mo and Cr compared to the austenitic matrix (Fig. 7 and Table 3). EDS measurements in TEM have also confirmed these Cr and Mo enrichment. Since they precipitate just after the disappearance of micro-segregation cells (enriched in Mo and Cr, as measured by Voisin et al. [13] and Birnbaum et al. [45]), there is a likely diffusion process of Mo and Cr atoms from micro-segregations to grain boundaries. Thus, these observations suggest that this particular diffusion phenomenon is thermally activated around 750°C - 800°C.

To confirm its possibility, simple chemical calculations have been realized by following the methodology presented in Smith's paper [53]. The diffusion distance of chromium in AISI 316 L was estimated at 0.3 μm for volume diffusion and 30 μm for grain boundary diffusion for a dwell time of 2 h at 800°C (considering a grain boundary thickness of 5 nm). As the mean grain size has been estimated at 20 μm based on EBSD measurements at the AB state, it can be concluded that diffusion length values are of the same order of magnitude as the diffusion length needed for Cr to precipitate at grain boundaries. These simple diffusion calculations confirm that Cr is able to diffuse along grain boundaries to form the precipitates.

Calculations are in good agreement with observations as grain boundaries are preferential precipitation sites (Fig. 6). Moreover, this hypothesis of heterogeneous nucleation is supported by a preferential precipitation at triple boundaries where larger precipitates can be observed in Fig. 6c.

For PMHTs at 1200 °C, intergranular precipitates are no longer visible at grain boundaries. To confirm observations in SEM, the local chemical composition was measured by EDS perpendicular to a grain boundary on a sample PMHT at 1200 °C (Fig. 7d). Fig. 7e reveals that there is no further enrichment (resp. depletion) in Cr and Mo (resp. Fe and Ni). All traces of chemical precipitation have disappeared from the grain boundaries after PMHT at 1200°C.
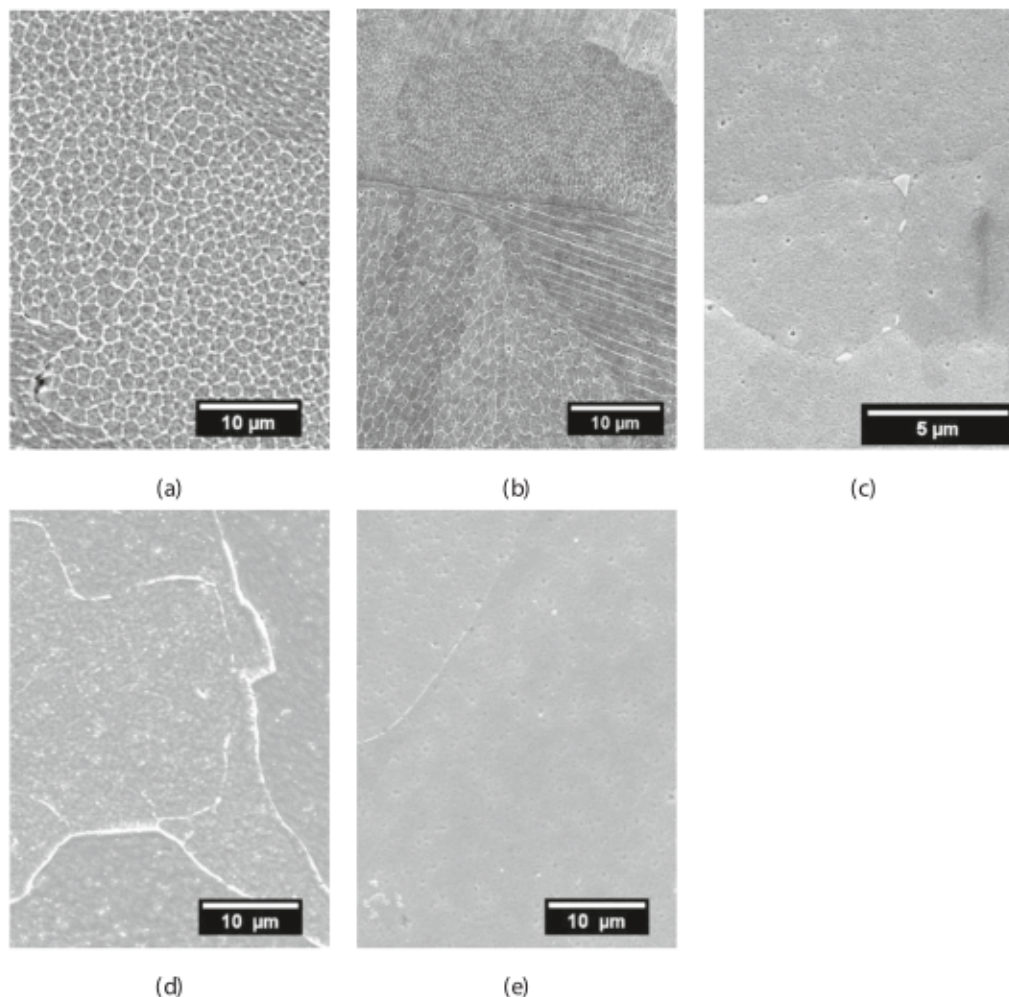
Fig. 6. SEM images after etching of samples PMHT at (a) 500 °C, (b) 650 °C, (c) 800 °C, (d) 1000 °C and (e) 1200 °C.

At these temperatures ([[800–1000°C]]), the formation of numerous phases is thermodynamically permissible. In the literature, carbides [41], the χ phase [54] and the σ phase [15,17] have already been observed after PMHTs in the same temperature range.

To determine the nature of the observed precipitates, TEM analyses were carried out on samples PMHT at 900°C (Fig. 8). First, TEM-EDS analysis confirmed the high Cr and Mo content in the intergranular precipitates as analyzed in SEM-EDS. Then, a diffraction pattern of the precipitate observed in Fig. 8a has been obtained (Fig. 8b). It has been identified as corresponding to the [132] zone axis of the σ phase structure ($P42/mnm$, $D4h14$, #136, ICSD ID102756) [55]. In conclusion, both chemical and crystallographic analyses conclude that the intergranular precipitates are σ phase precipitates.

This identification corresponds well with the disappearance of intergranular precipitates for PMHT above 1000°C, as observed in Fig. 6. Indeed, the sigma phase is not stable over this temperature range [56,57].

Sigma phase commonly precipitates for long exposure times at intermediate temperatures (700°C - 900°C; time > 100 h − 1000 h), from delta-ferrite islands first, then at triple boundaries and grain boundaries [55]. These preferential precipitation sites are due to the high Cr content that is needed to form the sigma phase [58]. Indeed, delta-ferrite is rich in Cr and grain boundaries act as a preferential diffusion path for Cr. However, no delta-ferrite was found by XRD or EBSD in this alloy in the AB state or after PMHT. This is in agreement with numerous studies on AM 316 L stainless steels [15,16,33,59]. The local high Cr content (> 20 wt%), necessary to form sigma-phase, comes from the fading of micro-

segregation cells, which occurs within the same temperature range. Cr then diffuses along grain boundaries and the sigma phase is able to precipitate.

According to the literature, the sigma phase has very slow precipitation kinetics and so should not be observed after PMHT for 2 h [55]. However, Parrens et al. [60] showed that these kinetics are accelerated under cycling ageing. As evidence of this, the content of sigma phase in a 310S alloy is far higher for cyclic ageing than for isothermal ageing (for the same exposure time at high temperature). The authors suggested that this phenomenon is associated with the residual stresses and dislocations – due to quenching during thermal cycling – that could become new nucleation sites for the sigma phase.

A parallel can then be drawn with the LPBF process: successive laser passes have a cyclic PMHT effect on the solidified material. This generates high residual stresses [61] and high dislocation density [44]. Thus, σ phase precipitation is favored and permitted for PMHT of just 2 h at constant temperature for 316 L LPBF steel. In the literature, Yin et al. [62] observed σ precipitation in a 316 L LPBF from 30 min of PMHT at 800 °C, Chao et al. [15] after 2 h of treatment at 800°C and Kurzynowski et al. [17] after 5 h at the same temperature.

Nevertheless, σ phase precipitation is rarely observed in the literature for 316 L LPBF steel. This is explained by the chemical composition of the powders. Indeed, Hsieh and Wu [58] have shown that increasing the nitrogen content from 0.03% to 0.14% delays the kinetics of sigma phase onset by an order of magnitude for a model 18Cr/11Ni/2Mo steel (close to the composition of 316 L). However, the powders used in our study have a very low nitrogen content (0.1%, see Table 1) compared
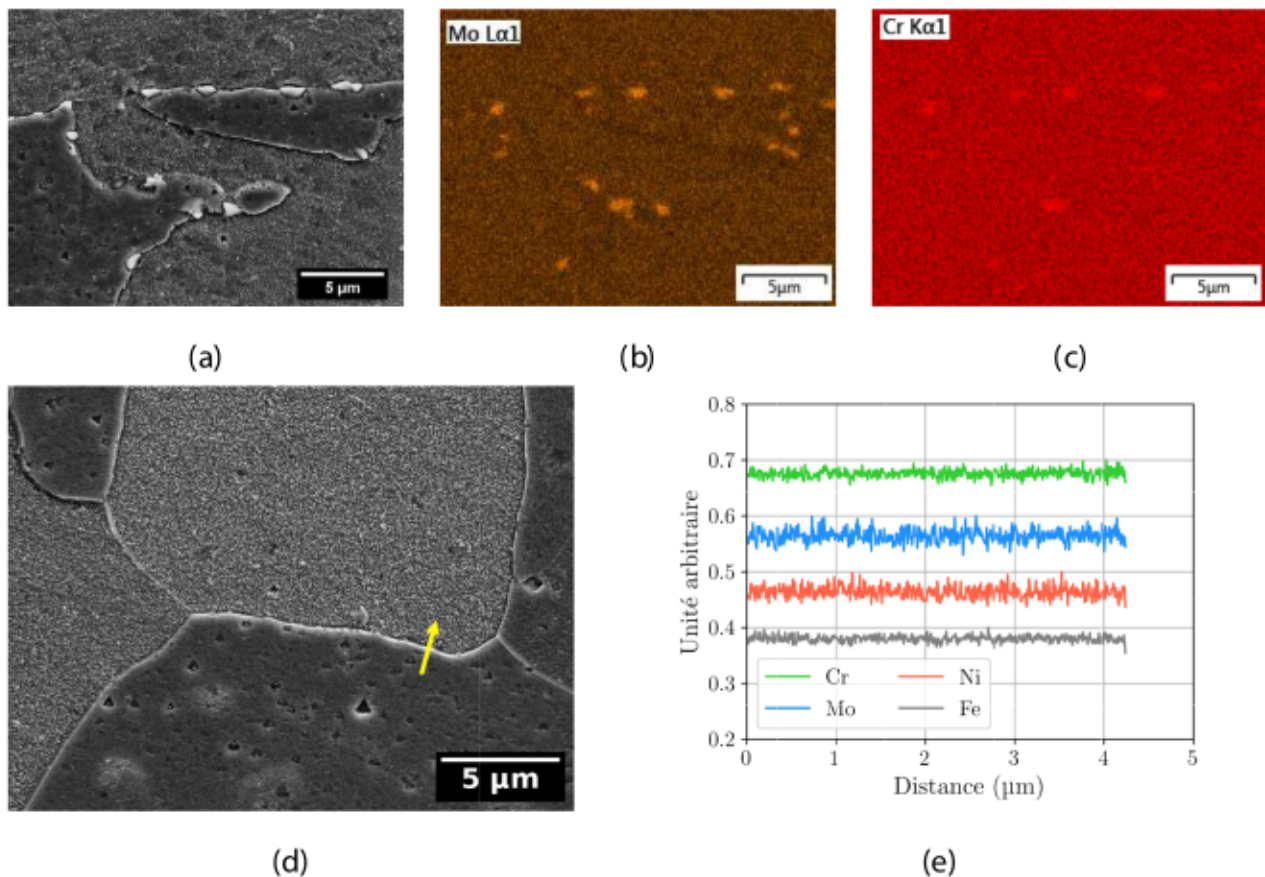
Fig. 7. SEM observation after etching of intergranular precipitates on a sample PMHT at (a-c) 900°C and (d-e) at 1200°C. (a) Secondary electron image, (b) Mo element map based on $L_{\alpha 1}$ signal and (c) Cr element map based on $K_{\alpha 1}$ signal. (d) shows the measurement line area of EDS profile (yellow arrow) on the sample PMHT at 1200°C and (e) is a plot of the chemical composition profiles obtained by EDS according to the yellow arrow. (For interpretation of the references to colour in this figure legend, the reader is referred to the web version of this article.)

Table 3

Chemical compositions of the matrix and precipitates measured by SEM-EDS and compared with the powder composition given by the powder supplier (Höganäs).

	Cr	Mo
Content in powder (from Höganäs, in *wt*%)	17.7	2.7
Content in austenitic matrix (*wt*%)	16.9	2.6
Content in precipitate (*wt*%)	24.6	10.0

with those in the literature. Voisin et al. [13] reported the nitrogen content of nine powders used in the literature, and found them to be at least three times higher than the nitrogen content of our powders. In publications reporting high nitrogen levels, no σ phase was observed after PMHTs, confirming the link between nitrogen content and σ phase precipitation.

4.3.2. Dislocation arrangements and density evolution with heat treatment temperature

Dislocation structures were studied by bright-field TEM for samples in the AB state, and after PMHT at 500, 650, 900 and 1200 °C.

The dislocation arrangement in cells was visible up to 900°C but not anymore at 1200°C. This result is in accordance with the literature, where the critical temperature at which dislocation cells vanish is around 800°C - 900°C [13]. However, very wide variations can be noted: a start of disappearance has been reported as early as 400 °C [59] while other authors report the existence of cells after PMHT at 1200 °C [19]. This dispersion implies that there is no exact critical temperature, but

rather a range of temperatures over which cells tend to disappear as supported by Kong et al. [8].

The average dislocation cell size (measured on TEM images) is shown in Table 4. There is an increase in cell size between the AB state and the PMHT at 500°C (approx. +40%), which is likely due to the diffusional annihilation of dislocation along the cell boundaries as supported by Chao et al. [15]. Cell size then remains constant at 0.57 μm on average up to 900°C. This constant size correlates well with Chen et al. [59], even though variations can be reported notably after PMHT. For example, Salman et al. [48] measured an increase in dislocation cell size from 0.52 μm at the AB temperature to 0.94 μm after PMHT at 600°C. These measurements must be taken with some care because they were performed by SEM after etching, and so, the cells observed are due to the micro-segregations and not directly to dislocations. This may explain the pointed differences. Chen et al. have measured dislocation cell sizes with TEM bright field images, agreed that there are no major variations in cell diameter between 400°C and 800°C [59].

Beyond cell size, cell boundaries thickness is also subject to change. In the AB state and at 500°C, cell boundaries are thick (approx. 100 nm - 200 nm) and full of dislocations (Fig. 9c), whereas they are very fine (approx. 10 nm - 20 nm) after PMHT above 650°C (Fig. 9d). This observation confirms the work done by Voisin et al. which support that PMHTs decrease dislocation density in cell boundaries [13].

TEM bright field images can however be misleading due to the orientation of crystal lattice and the thickness of TEM lamella can alter the ability to observe dislocations in bright field. In order to confirm the TEM observations, dislocation density was calculated thanks to XRD measurements (Fig. 9g). Fig. 9g presents the evolution of dislocation density wit PMHT temperature. Methodology is presented in 2 section. It
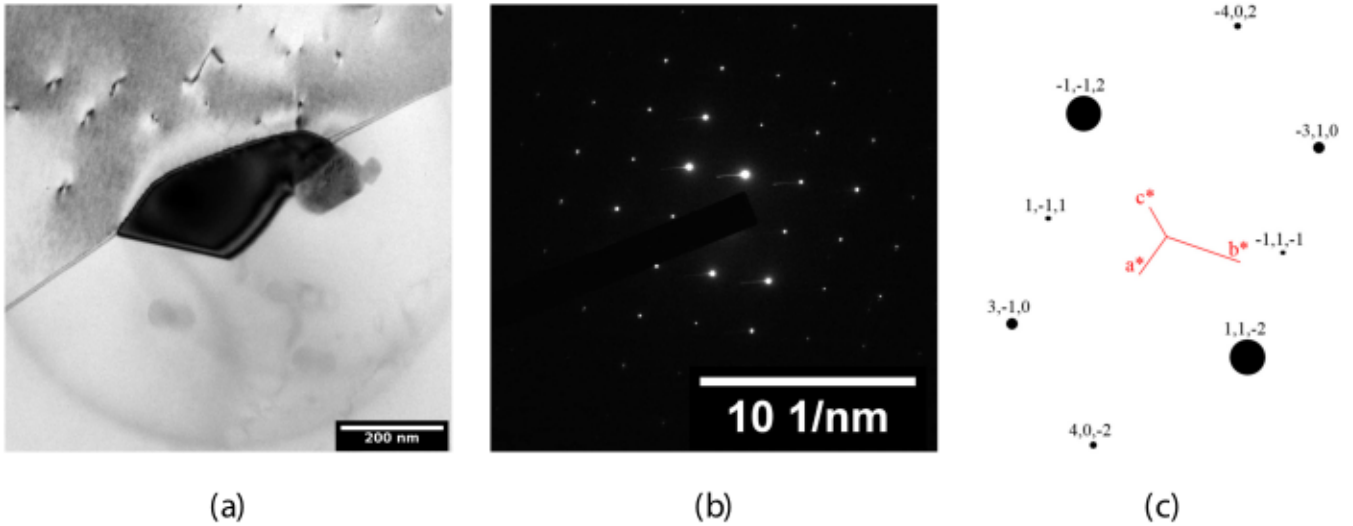
Fig. 8. TEM observation of intergranular precipitates on a sample PMHT at 900 °C: (a) Bright-field image of an intergranular precipitate, (c) diffraction pattern of the precipitate and (d) identification of the diffraction pattern.

Table 4
Average dislocation cell diameter evolution with PMHTs. Based on TEM bright field observations.

PMHT	AB	500C	650C	900C
Dislocation cell diameter (µm)	0.42 ± 0.04	0.60 ± 0.02	0.55 ± 0.03	0.57 ± 0.05

shows an initial stage of stability up to 650°C. Indeed, the slight increase is more probably related to inaccuracies in the quantification than to the material evolution. Then, there is a decrease in dislocation density up to 1200°C. These measurements allow the conclusions from TEM observations to be nuanced. The decrease in dislocation density suggested by TEM images between 500°C and 650°C is probably not so evident.

Above 650°C, dislocation density declines until 1200°C (− 64%). This is in accordance with TEM suggestions. Therefore, this decline in dislocation density is very likely related to a static recovery [52]. However, the decrease in dislocation density is relatively low for a static recovery. It is explained by the calculation method used, which do not consider differences between edge or screw dislocations. It is only based on a Pseudo-Voigt model fit with the diffraction peaks in order to evaluate their Lorentzian (width related to crystallite size) and Gaussian (width related to micro-strains) contributions. Therefore, recovery effect is very likely under-estimated.

Nevertheless, the literature confirms the dislocation density calculated at the AB state from XRD measurements. Bertsch et al. calculated a comparable dislocation density at the AB state (10^{14} m^{-2}) with the intercept line technique on TEM images [44]. Gorsse et al. have estimated the AB dislocation density to 4.10^{14} m^{-2} which correspond to the value determined by XRD in this study [63].

Finally, the coupled analysis between TEM and XRD provides confidence into the results. Comparing TEM and XRD analysis, the following conclusions regarding dislocations evolution with PMHT can be drawn:

1. Below 600°C, there are no major variations in dislocation density and arrangements, conserving a high density of dislocations in cell walls.
2. Then, from 600°C to 900°C the cell boundary thickness decreases, resulting in a dislocation density drop.
3. Above 900°C, the remaining dislocations slowly vanish and the dislocation network disappears.

4.3.3. Nano-oxide size and morphology evolution with heat treatment temperature

TEM analysis were carried out on thin foils extracted from samples in the AB state and heat treated at 500, 650, 900 and 1200°C. As an example, an image realized on each sample is available in Fig. 10. In these images, the nano-oxides have been outlined in blue for better visibility. The surface fraction occupied by nano-oxides doesn't show significant variation with PMHT temperature and has been calculated at 1%. Higher magnification images of precipitates are available in Fig. 11.

The average diameter of the nano-oxides was measured on all the images taken for the different samples and plotted with the PMHT temperature (Fig. 11c). While the average size of the precipitates remains relatively contained up to 650°C (+52% compared with the AB state), it then increases sharply to 115 nm after PMHT at 1200°C (+570% compared with the AB state).

This sharp increase in size takes place over temperature ranges where diffusion processes have been demonstrated at higher scales (see section 4.3). It is therefore highly probable that chemical diffusion takes place between precipitates, favoring the growth of larger precipitates to the detriment of smaller ones. This mechanism, similar to *Ostwald ripening* [64], can be explained quite simply by considering that the disappearance of small precipitates in favor of large ones minimizes the interface surface area and therefore the internal energy of the material.

Similar results exist in the literature [20,23]. In particular, Deng et al. [20] show a coarsening of nano-oxides for PMHTs above 900 °C and a decrease in their density. They also attribute this phenomenon to a *Ostwald ripening* mechanism.

In the AB state, the nano-oxide particles structure characterization was not always conclusive due to the small size of these spherical particles. However, high-resolution TEM images (as seen in Fig. 11a) show the presence of a crystal structure, whatever the size of the precipitates. The crystal structure of these nano-oxides could correspond to the one identified by Yan et al. [19], namely a metastable rhodonite-type structure. The chemical compositions of ten nano-oxide particles were analyzed by MET-EDS. A quantitative analysis was not possible. However, the presence of certain elements in the nano-oxides could be investigated. It was found that small nano-oxides (5 to 15 nm) are made of the same elements as the large nano-oxides (> 50 nm): mainly Mn, Si and rarely Cr. According to Yan et al. study [19], they are mainly $MnSiO_3$ rhodonite structure (9/10) and sometimes $MnCr_2O_4$ spinnel structure (1/10).

Beyond size evolution, morphology of precipitates also changes with PMHT temperature. Two different shapes have been reported, spherical
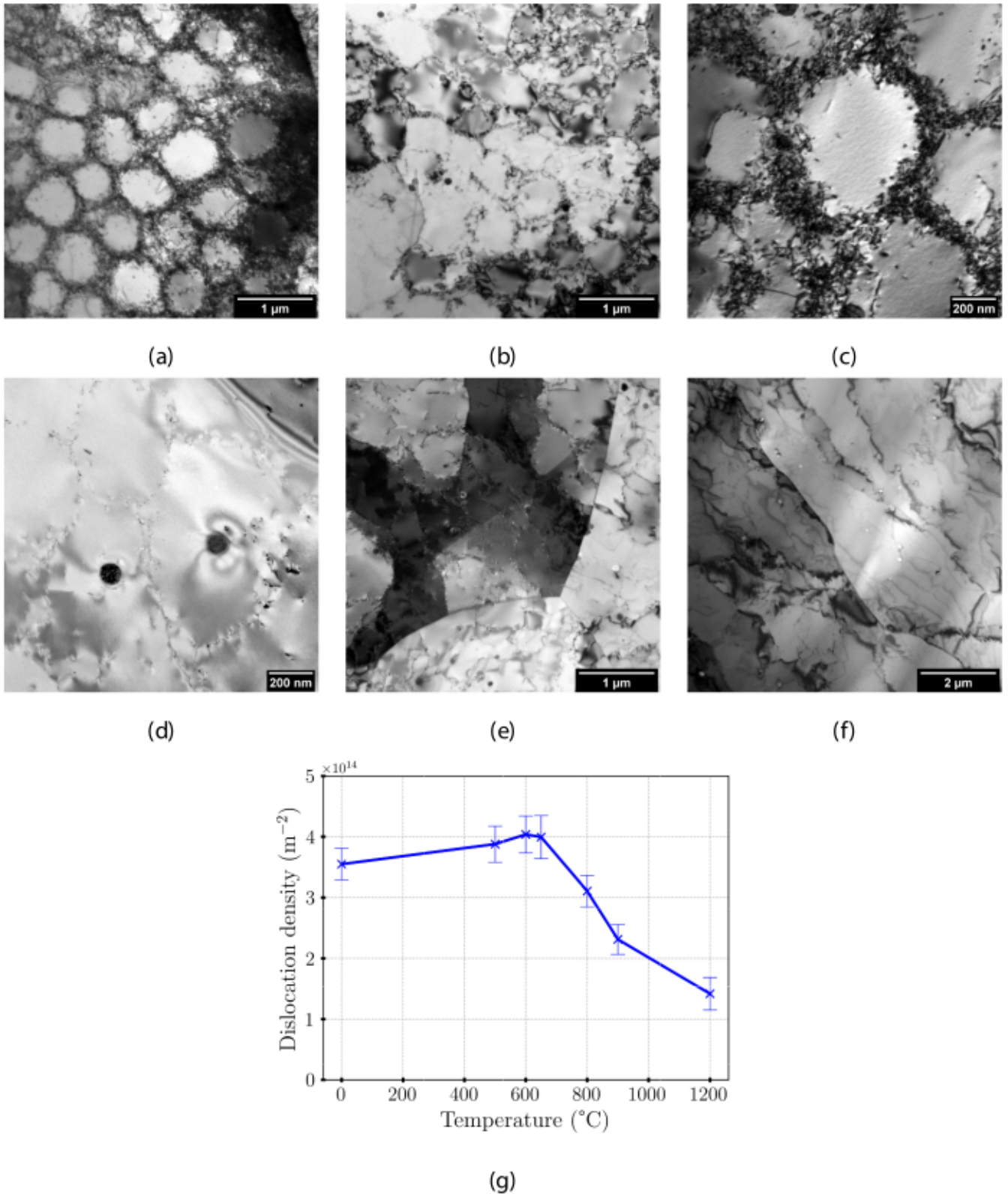
Fig. 9. Coupled analysis of dislocation structures and density evolution with temperature. (a-f) Bright field images of samples heat treated at (a,c) 500 °C, (b,d) 650 °C, (e) 900 °C and (f) 1200 °C. (g) Dislocation density evolution with PMHT temperature.

and prismatic (Fig. 11). All the precipitates observed are spherical in the AB state. Then, a gradual prismatization of nano-oxides is thus observed between the AB and 1200 °C states. This morphological evolution is linked to a change in crystalline structure as suggested by Yan et al. [19] from $MnSiO_3$ rhodonite type structure to $MnCr_2O_4$ spinel type structure.
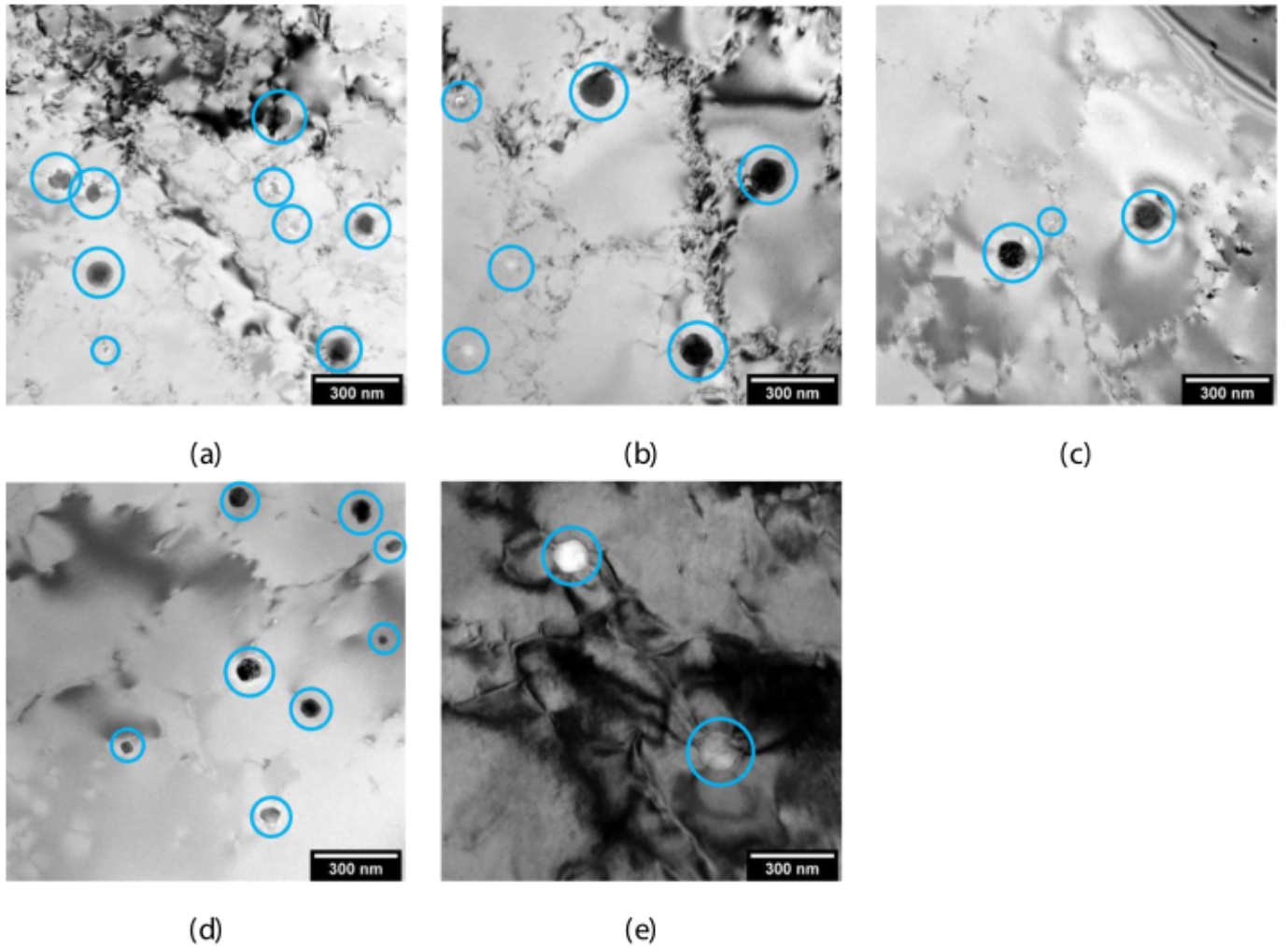
Fig. 10. Bright field TEM images showing nano-oxides at the (a) AB, and after PMHT at (b) 500 °C, (c) 650 °C, (d) 900 °C et (e) 1200 °C.

4.4. Multiscale correlation between heat treated microstructure and tensile properties

4.4.1. Evolution of tensile properties

This part aims at relying on the evolution of multiscale microstructure to modifications of tensile properties after PMHTs. Fig. 12 describes these evolutions.

Yield strength (σ_e, calculated at 0.2% strain) decreases sharply (−31%), while maximum strength (σ_m) decreases slightly (−6%), elongation at failure (ε_r) increases by 33% and uniform elongation (ε_u) increases by 65% between the AB state and the PMHT at 1200 °C. These trends reflect a decrease in strength as well as an increase in ductility with PMHTs.

More specifically, between the AB and 500 °C states, there is a 16% increase in elongation at break without any significant decrease in mechanical strength (σ_e -4%, σ_m +3%). This PMHT corresponds to the best strength/ductility compromise obtained in this study.

Between the AB and 1200 °C states, yield strength decreases by >30%, while maximum strength decreases by only 6%. As a result, the ratio σ_e/σ_m decreases linearly from 0.79 in the AB condition to 0.56 at 1200 °C. High values (>0.7) of this ratio are typical of LPBF materials, due to the high dislocation densities they contain in the AB state. This results in relatively low strain-hardening capacities. The decline in this ratio shows that the strain-hardening rate increases with temperature, as demonstrated by Voisin et al. [13].

In order to estimate the evolution of strain hardening capabilities,

the parameter n defined by eq. 6, with ε_u the uniform elongation, was calculated for each tensile test and plotted on Fig. 12c.

$$n = \frac{\sigma_m - \sigma_e}{\varepsilon_u} \qquad (6)$$

Three distinct trends have been identified:

1. Between the AB state and 500 °C, strain-hardening is low. PMHT at 500 °C does not significantly modify strain-hardening capabilities. This is consistent with the evolution of dislocation cells: no change in dislocation density (determined by XRD, or observed in cell walls by TEM) was noted.
2. Between 600 and 800°C, strain-hardening capabilities increase sharply. This corresponds to the disappearance of the dislocation cell network, and more precisely, to the sharp decrease in dislocation densities in the cell walls.
3. Between 900 and 1200°C, strain-hardening capabilities are constant. Only a few dislocations remain in the microstructure, and their disappearance doesn't modify the strain-hardening capacity.

Finally, despite the high dislocation density (particularly in the cell walls), 316 L LPBF steel has a reasonable strain-hardening capacity in the AB state. Zhu et al. explains the good work-hardening capacity of LPBF as-built materials by the hierarchical microstructure providing a substantial strengthening contribution [65]. The authors explain that dislocation cells structures play a crucial role in maintaining work-hardening capacity because they are not traditional dislocation walls
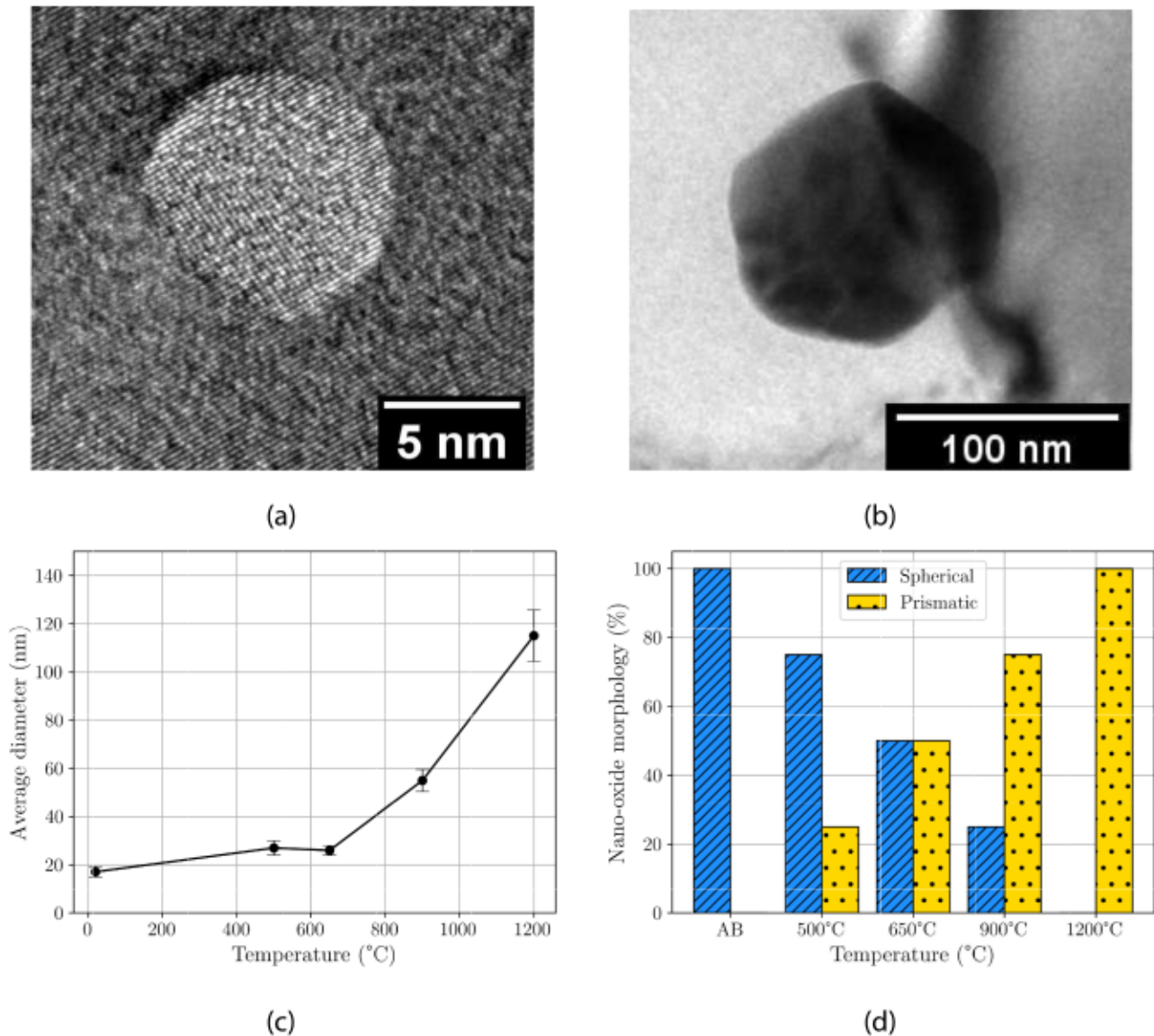
Fig. 11. Examples of nano-oxides observed by TEM in (a) the AB state (spherical form) and (b) after PMHT at 900°C (prismatic form). (c) shows the average diameter evolution and (d) the average evolution of precipitate morphology.

[66]. These dislocation cells can trap and store high dislocation density. The authors finally showed that interactions between slip bands and these cellular structures result in the formation of a sophisticated dislocation configuration that ultimately blocks dislocation motion like conventional high angle grain boundaries (HAGBs) [66].

In contrast, after high-temperature PMHTs, the initial dislocation density is low. As a result, many dislocations can be generated to accommodate deformation during the tensile test. This physical mechanism then results in higher strain-hardening capacities, enabling maximum strengths comparable to those in the AB state to be achieved.

4.4.2. Multiscale microstructural contribution

On a macroscopic scale, no significant changes in grain size were observed. The contribution of grain boundaries (through a Hall-Petch effect) does not therefore play a part in tensile evolution. On the contrary, at micro and nanoscopic scales, significant changes in microstructure have been observed. The following paragraphs provide an assessment of their contributions.

4.4.2.1. On the mechanical strength. Yield strength can be related to

variations in nano-oxide sizes and dislocation densities (Fig. 13a). Methodology to estimate their contribution is depicted in section 2.

Figure 13a shows that dislocations highly contribute to yield strength: from 250 MPa at the AB state to 150 MPa after PMHT at 1200°C. On all the PMHT range, it represents 55 to 75% of total yield strength.

Otherwise, the nano-oxides contribution is lower than dislocations independently of PMHT: from 150 MPa at the AB state to 25 MPa after the 1200°C PMHT.

The sum of these two contributions is compared to yield strength evolution relatively to the AB state (Fig. 13b). A very good agreement is obtained for PMHTs below 900 °C. Moreover, the absolute prediction is also good as the sum of these two contributions represents >80% of the yield strength for PMHTs on this temperature range.

Consequently, grain boundary hardening (Hall-Petch effect) or solid solution hardening account for only 20% (maximum) of the yield strength for 316 L LPBF alloy at PMHTs below 900 °C. Therefore, it underlines the necessity to study both micro and nanoscale of the microstructure to predict mechanical properties, as realized in this paper.
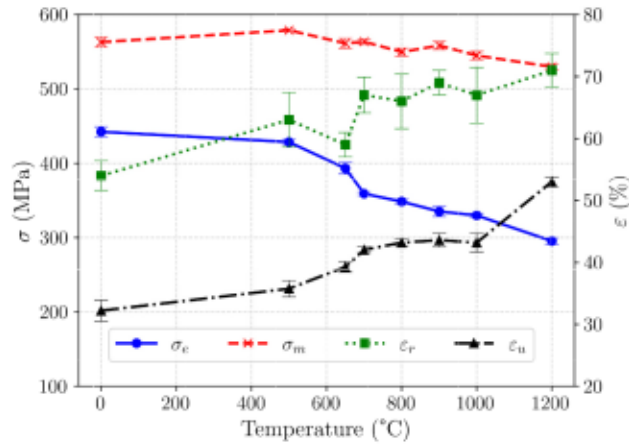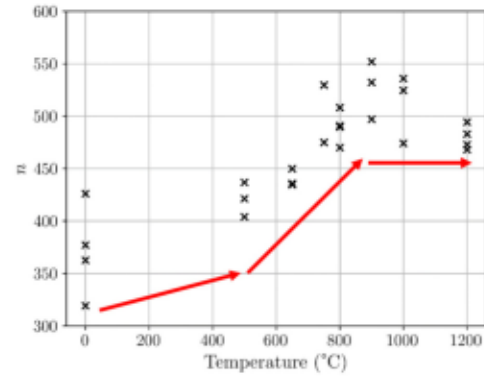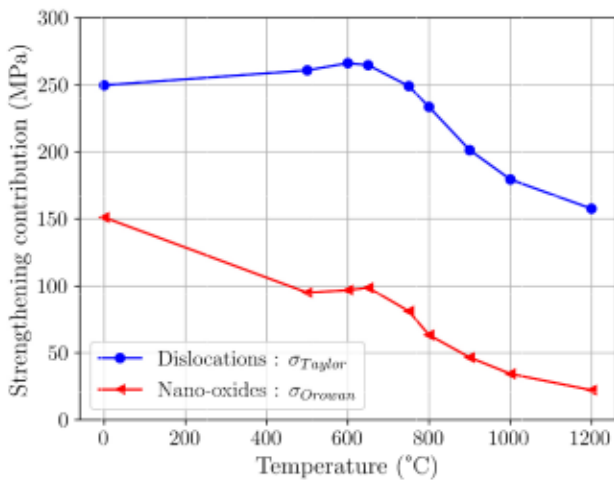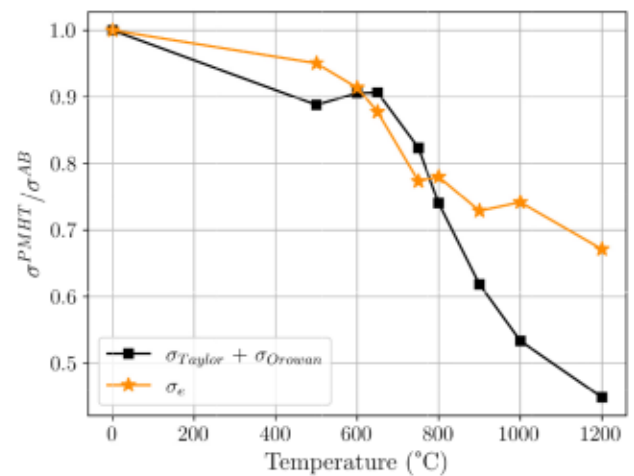
(a)
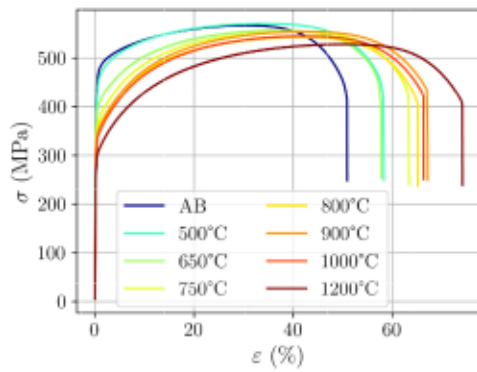
(b)

(c)

Fig. 12. (a) Tensile properties (σ_e the yield strength, σ_m the ultimate tensile strength, ε_r the conventional failure elongation and ε_u the uniform elongation) evolution with PMHT temperature, (b) examples of tensile curves after each PMHT and (c) evolution of a simplified strain hardening capabilities parameter with PMHT temperature.

(a)

(b)

Fig. 13. (a) Estimated contribution of nano-oxides (σ_{Orowan}) and dislocations (σ_{Taylor}) to alloy strength with PMHT temperature, and (b) normalized evolution of both contribution of nano-oxides and dislocations to yield strength σ_e.

At higher temperatures, the agreement between model predictions and yield strength decreases sharply as shown by Fig. 13b. Given the great complexity of the hierarchical microstructure, it was obvious that the models would be too simplistic to correctly predict mechanical properties over the entire PMHT temperature range. The discrepancies at high PMHT temperatures can be explained by the following two assumptions:

- The Taylor and/or Orowan models do not correctly describe the contribution of dislocations and/or nano-oxides over this temperature range. Above 800–900°C, the arrangement of dislocations into a cellular network disappears, and the remaining dislocations become more disordered. Their contribution to hardening is most likely modified.
- Re-solution of sigma phase precipitates above 1000°C could increase solid solution hardening and thus contribute to further alloy hardening. However, this hypothesis cannot be verified at present.

In the literature, above 1000°C, Ronneberg et al. [47] and Voisin et al. [13] attribute the final yield stress decrease to recrystallization. However, no recrystallization was observed in our case (section 4.2.2), and the Taylor and Orowan models predict a sharp decrease in yield strength between 1000 and 1200 °C. Therefore, our paper sheds new light on this hypothesis and further highlights two phenomena to explain the significant loss of yield strength between 1000 and 1200°C: the total disappearance of process-induced dislocations and the coarsening of nano-oxides.

4.4.2.2. On the failure elongation. Elongation at break increases rather linearly between the AB and 1200 °C states. However, intergranular precipitation of sigma phase was observed between 800 and 1000 °C. This phase, when located at grain boundaries, is known to have an embrittling effect on conventional stainless steels [58]. However, no reduction in elongation at break was observed in our study.

In the literature, Chao et al. [15] also observed σ phase precipitation for PMHTs at 800°C on a 316 L LPBF steel. This precipitation, although low (0.11% by volume), is associated with a sharp decrease in failure elongation. Therefore, in their case, 316 L LPBF steel does not appear to be less susceptible to sigma-phase embrittlement than its forged counterpart.

However, these observations do not match the behavior reported in Fig. 12a and b for our alloy. The size and positions of the sigma phases appear to be comparable between our study and that of Chao et al. [15]. In our case, the rate of sigma phase has not been precisely quantified, but it is <2% since this phase has not been detected by XRD.

In conclusion, contrary to most literature, Fig. 12 shows that the σ phase, even intergranular, is not necessarily detrimental to the failure elongation of 316 L LPBF steel.

5. Conclusions

An in-depth study of the effects of PMHTs on multiscale microstructure of 316 L LPBF steel was carried out. This led to the following conclusions, summarized by the Fig. 14:

1. At the polycrystalline scale

- Grain boundaries are stable up to 1200°C. No recrystallization has been observed contrary of most of the studies in the terature.
- Melt-pools boundaries disappear between 800 and 1000 °C. Their disappearance is linked to chemical diffusion processes at lower scales.

2. At the microscopic scale

- Micro-segregations disappear around 750°C. Then, Cr/Mo diffuse at grain boundaries to precipitate into σ phase in <2 h, due to low nitrogen content. σ phase then dissolves up to 1000°C. This paper helps at explaining the absence of σ phase precipitation for most literature studies compared to this one.
- Dislocation cells grow between 500 and 650 °C. Then, from 600 °C, the density of dislocations in the cell walls decreases. There is no exact temperature at which the cellular network of dislocations disappears, but rather a sharp decrease in its intensity between 600 and 900°C.

3. At the nanoscopic scale

- The size of nano-oxides increases significantly with PMHT temperature, especially from 900°C to 1200°C. On the entire temperature range, they show a gradual modification of their crystalline structure (resp. morphology) rhodonite (resp. spherical) to spinnel (resp. prismatic).

Contributions to alloy strengthening on all the PMHT temperature range [0–1200°C] have been estimated for microscopic and nanoscopic scales. The following main conclusions can be drawn:

- Dislocations networks and nano-oxides are mainly responsible for the high tensile properties of 316 L LPBF steel at the AB state and after PMHT below 900°C. The contribution of nano-oxides to yield strength highly decreases at high temperatures.
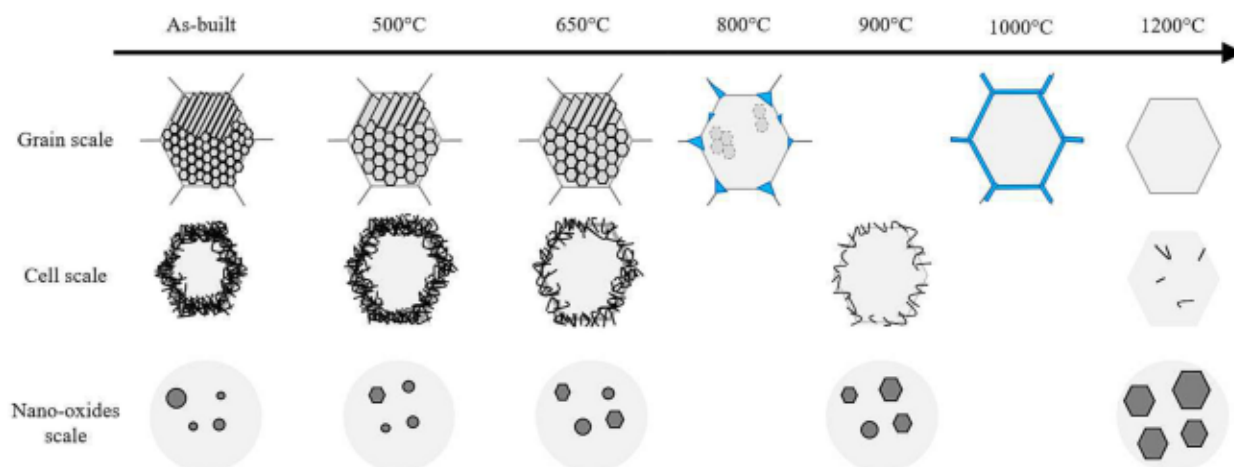

Fig. 14. Multiscale microstructure evolution with PMHT temperature.

- Orowan/Taylor models can predict with a good agreement yield strength on the [0–800°C] temperature range. However, they are too simplistic to take into account for multiscale microstructure evolutions above 900°C.
- The σ phase does not necessarily have a detrimental effect on failure elongation for 316 L LPBF steel, contrary to what is usually reported in the literature.

CRediT authorship contribution statement

Hugo Roirand: Conceptualization, Formal analysis, Investigation, Methodology, Validation, Visualization, Writing – original draft. **Alessandro Pugliara:** Formal analysis, Methodology, Writing – review & editing. **Benoit Malard:** Formal analysis, Methodology, Supervision, Validation, Writing – review & editing. **Anis Hor:** Investigation, Methodology, Supervision, Writing – review & editing. **Nicolas Saintier:** Formal analysis, Methodology, Supervision, Writing – review & editing.

Declaration of Competing Interest

The authors declare that they have no known competing financial interests or personal relationships that could have appeared to influence the work reported in this paper.

Data availability

Data will be made available on request.

Acknowledgements

References

[1] M. Santamaria, G. Tranchida, F. Di Franco, Corrosion resistance of passive films on different stainless steel grades in food and beverage industry, Corros. Sci. 173 (2020), 108778, https://doi.org/10.1016/j.corsci.2020.108778.

[2] Y. Dai, X. Zheng, P. Ding, Review on sodium corrosion evolution of nuclear-grade 316 stainless steel for sodium-cooled fast reactor applications, Nucl. Eng. Technol. 53 (11) (2021) 3474–3490, https://doi.org/10.1016/j.net.2021.05.021.

[3] T. DebRoy, H. Wei, J. Zuback, T. Mukherjee, J. Elmer, J. Milewski, A. Beese, A. Wilson-Heid, A. De, W. Zhang, Additive manufacturing of metallic components – process, structure and properties, Prog. Mater. Sci. 92 (2018) 112–224, https://doi.org/10.1016/j.pmatsci.2017.10.001.

[4] A. Racot, I. Aubert, M. Touzet, S. Thiebaut, M. Demesy, Statistical analysis of the pitting corrosion induced by potentiostatic pulse tests of wrought and slm 316l stainless steels, Corros. Sci. 197 (2022), 110036, https://doi.org/10.1016/j.corsci.2021.110036.

[5] S. Bahl, S. Mishra, K. Yazar, I.R. Kola, K. Chatterjee, S. Suwas, Non-equilibrium microstructure, crystallographic texture and morphological texture synergistically result in unusual mechanical properties of 3d printed 316l stainless steel, Addit. Manuf. 28 (2019) 65–77, https://doi.org/10.1016/j.addma.2019.04.016.

[6] X. Wang, J.A. Muñiz-Lerma, M. Attarian Shandiz, O. Sanchez-Mata, M. Brochu, Crystallographic-orientation-dependent tensile behaviours of stainless steel 316l fabricated by laser powder bed fusion, Mater. Sci. Eng. A 766 (2019), 138395, https://doi.org/10.1016/j.msea.2019.138395.

[7] S.-H. Sun, T. Ishimoto, K. Hagihara, Y. Tsutsumi, T. Hanawa, T. Nakano, Excellent mechanical and corrosion properties of austenitic stainless steel with a unique crystallographic lamellar microstructure via selective laser melting, Scr. Mater. 159 (2019) 89–93, https://doi.org/10.1016/j.scriptamat.2018.09.017.

[8] D. Kong, About metastable cellular structure in additively manufactured austenitic stainless steels, Addit. Manuf. (2021) 23.

[9] Y.M. Wang, T. Voisin, J.T. McKeown, J. Ye, N.P. Calta, Z. Li, Z. Zeng, Y. Zhang, W. Chen, T.T. Roehling, R.T. Ott, M.K. Santala, P.J. Depond, M.J. Matthews, A. V. Hamza, T. Zhu, Additively manufactured hierarchical stainless steels with high strength and ductility, Nat. Mater. 17 (1) (2018) 63–71, https://doi.org/10.1038/nmat5021.

[10] B. Barkia, P. Aubry, P. Haghi-Ashtiani, T. Auger, L. Gosmain, F. Schuster, H. Maskrot, On the origin of the high tensile strength and ductility of additively manufactured 316L stainless steel: multiscale investigation, J. Mater. Sci. Technol. 41 (2020) 209–218, https://doi.org/10.1016/j.jmst.2019.09.017. https://hal.science/hal-02363398.

[11] D.J. Sprouster, W. Streit Cunningham, G.P. Halada, H. Yan, A. Pattammattel, X. Huang, D. Olds, M. Tilton, Y.S. Chu, E. Dooryhee, G.P. Manoghan, J.

[12] Z. Liu, D. Zhao, P. Wang, M. Yan, C. Yang, Z. Chen, J. Lu, Z. Lu, Additive manufacturing of metals: microstructure evolution and multistage control, J. Mater. Sci. Technol. 100 (2022) 224–236, https://doi.org/10.1016/j.jmst.2021.06.011.

[13] T. Voisin, J.-B. Forien, A. Perron, S. Aubry, N. Bertin, A. Samanta, A. Baker, Y. M. Wang, New insights on cellular structures strengthening mechanisms and thermal stability of an austenitic stainless steel fabricated by laser powder-bed-fusion, Acta Mater. 203 (2021), 116476, https://doi.org/10.1016/j.actamat.2020.11.018.

[14] D. Riabov, A. Leicht, J. Ahlström, E. Hryha, Investigation of the strengthening mechanism in 316l stainless steel produced with laser powder bed fusion, Mater. Sci. Eng. A 822 (2021), 141699, https://doi.org/10.1016/j.msea.2021.141699.

[15] Q. Chao, S. Thomas, N. Birbilis, P. Cizek, P.D. Hodgson, D. Fabijanic, The effect of post-processing heat treatment on the microstructure, residual stress and mechanical properties of selective laser melted 316l stainless steel, Mater. Sci. Eng. A 821 (2021), 141611, https://doi.org/10.1016/j.msea.2021.141611.

[16] J. Lei, Y. Ge, T. Liu, Z. Wei, Effects of heat treatment on the microstructure and mechanical properties of selective laser melting 316l stainless steel, Shock. Vib. 2021 (2021) 1–12, https://doi.org/10.1155/2021/6547213.

[17] T. Kurzynowski, K. Gruber, W. Stopyra, B. Kuźnicka, E. Chlebus, Correlation between process parameters, microstructure and properties of 316 l stainless steel processed by selective laser melting, Mater. Sci. Eng. A 718 (2018) 64–73, https://doi.org/10.1016/j.msea.2018.01.103.

[18] K. Saeidi, L. Kvetková, F. Lofaj, Z. Shen, Austenitic stainless steel strengthened by the in situ formation of oxide nanoinclusions, RSC Adv. 5 (27) (2015) 20747–20750, https://doi.org/10.1039/C4RA16721J.

[19] F. Yan, W. Xiong, E. Faierson, G.B. Olson, Characterization of nano-scale oxides in austenitic stainless steel processed by powder bed fusion, Scr. Mater. 155 (2018) 104–108, https://doi.org/10.1016/j.scriptamat.2018.06.011.

[20] P. Deng, M. Song, J. Yang, Q. Pan, S. McAllister, L. Li, B.C. Prorok, X. Lou, On the thermal coarsening and transformation of nanoscale oxide inclusions in 316l stainless steel manufactured by laser powder bed fusion and its influence on impact toughness, Mater. Sci. Eng. A 835 (2022), 142690, https://doi.org/10.1016/j.msea.2022.142690.

[21] Y. Miao, K. Mo, Z. Zhou, X. Liu, K.-C. Lan, G. Zhang, M.K. Miller, K.A. Powers, Z.-G. Mei, J.-S. Park, J. Almer, J.F. Stubbins, On the microstructure and strengthening mechanism in oxide dispersion-strengthened 316 steel: a coordinated electron microscopy, atom probe tomography and in situ synchrotron tensile investigation, Mater. Sci. Eng. A 639 (2015) 585–596, https://doi.org/10.1016/j.msea.2015.05.064.

[22] D. Kong, C. Dong, X. Ni, L. Zhang, H. Luo, R. Li, L. Wang, C. Man, X. Li, The passivity of selective laser melted 316l stainless steel, Appl. Surf. Sci. 504 (2020), 144495, https://doi.org/10.1016/j.apsusc.2019.144495.

[23] E. Ura-Bińczyk, A. Dobkowska, P. Bazarnik, J. Ciftci, A. Krawczyńska, W. Chromiński, T. Wejrzanowski, R. Molak, R. Sitek, T. Płociński, J. Jaroszewicz, J. Mizera, Effect of annealing on the mechanical and corrosion properties of 316l stainless steel manufactured by laser powder bed fusion, Mater. Sci. Eng. A 860 (2022), 144263, https://doi.org/10.1016/j.msea.2022.144263.

[24] E. de Sonis, S. Dépinoy, P.-F. Giroux, H. Maskrot, P. Wident, O. Hercher, F. Villaret, A.-F. Gourgues-Lorenzon, Microstructure – toughness relationships in 316L stainless steel produced by laser powder bed fusion, Mater. Sci. Eng. A 877 (2023) 145179, https://doi.org/10.1016/j.msea.2023.145179. https://linkinghub.elsevier.com/retrieve/pii/S0921509323006032.

[25] AFNOR, Nf en 10028–7, 2016.

[26] B. Beausir, J.-J. Fundenberger, Analysis Tools for electron and x-Ray Diffraction, Atex-Software, 2017.

[27] P.-U. Sonis, S. Dépinoy Edouard, P.-F. Giroux, H. Maskrot, L. Lemarquis, O. Hercher, F. Villaret, A.-F. Gourgues-Lorenzon, Dependency of recrystallization kinetics on the solidification microstructure of 316l stainless steel processed by laser powder bed fusion (lpbf), Mater. Charact. 194 (2022) 112370, https://doi.org/10.1016/j.matchar.2022.112370.

[28] C. Boudias, D. Monceau, Carine crystallography 3.1 (c), URL, http://carine, 1989, crystallography.pagesperso-orange.fr.

[29] H.M. Rietveld, A profile refinement method for nuclear and magnetic structures, J. Appl. Crystallogr. 2 (2) (1969) 65–71, https://doi.org/10.1107/S0021889869006558.

[30] G. Williamson, W. Hall, X-ray line broadening from filed aluminium and wolfram, Acta Metall. 1 (1) (1953) 22–31, https://doi.org/10.1016/0001-6160(53)90006-6.

[31] V. Mote, Y. Purushotham, B. Dole, Williamson-hall analysis in estimation of lattice strain in nanometer-sized zno particles, J. Theor. Appl. Phys. 6 (1) (2012) 6, https://doi.org/10.1186/2251-7235-6-6.

[32] X. Wang, J.A. Muñiz-Lerma, O. Sánchez-Mata, M. Attarian Shandiz, M. Brochu, Microstructure and mechanical properties of stainless steel 316l vertical struts manufactured by laser powder bed fusion process, Mater. Sci. Eng. A 736 (2018) 27–40, https://doi.org/10.1016/j.msea.2018.08.069.

[33] M. Godec, S. Zaefferer, B. Podgornik, M. Šinko, E. Tchernychova, Quantitative multiscale correlative microstructure analysis of additive manufacturing of stainless steel 316l processed by selective laser melting, Mater. Charact. 160 (2020), 110074, https://doi.org/10.1016/j.matchar.2019.110074.

[34] S. Dépinoy, Influence of solidification conditions on chemical heterogeneities and dislocations patterning in additively manufactured 316l stainless steel, Materialia 24 (2022), 101472, https://doi.org/10.1016/j.mtla.2022.101472.

[35] G.-I. Shamsujjoha Md, S.R. Agnew, J.M. Fitz-Gerald, W.R. Moore, T.A. Newman, High strength and ductility of additively manufactured 316l stainless steel explained, Metall. Mater. Trans. A 49 (7) (2018) 3011–3027, https://doi.org/10.1007/s11661-018-4607-2.

[36] N. Chen, G. Ma, W. Zhu, A. Godfrey, Z. Shen, G. Wu, X. Huang, Enhancement of an additive-manufactured austenitic stainless steel by post-manufacture heat-treatment, Mater. Sci. Eng. A 759 (2019), https://doi.org/10.1016/j.msea.2019.04.111.

[37] M. Odnobokova, V. Torganchuk, M. Tikhonova, P. Dolzhenko, R. Kaibyshev, A. Belyakov, On the strength of a 316l-type austenitic stainless steel produced by selective laser melting, Metals 13 (8) (2023), https://doi.org/10.3390/met13081423. URL: https://www.mdpi.com/2075-4701/13/8/1423.

[38] M. Zhang, Y. Tian, X. Zheng, Y. Zhang, L. Chen, J. Wang, Research progress on multi-component alloying and heat treatment of high strength and toughness al–si–cu–mg cast aluminum alloys, Materials 16 (2023) 1065, https://doi.org/10.3390/ma16031065.

[39] O. Andreau, I. Koutiri, P. Peyre, J.-D. Penot, N. Saintier, E. Pessard, T. De Terris, C. Dupuy, T. Baudin, Texture control of 316l parts by modulation of the melt pool morphology in selective laser melting, J. Mater. Process. Technol. 264 (2019) 21–31, https://doi.org/10.1016/j.jmatprotec.2018.08.049.

[40] M.-S. Pham, B. Dovgyy, P.A. Hooper, C.M. Gourlay, A. Piglione, The role of side-branching in microstructure development in laser powder-bed fusion, Nat. Commun. 11 (1) (2020) 749, https://doi.org/10.1038/s41467-020-14453-3.

[41] C. Man, Z. Duan, Z. Cui, C. Dong, D. Kong, T. Liu, S. Chen, X. Wang, The effect of sub-grain structure on intergranular corrosion of 316l stainless steel fabricated via selective laser melting, Mater. Lett. 243 (2019) 157–160, https://doi.org/10.1016/j.matlet.2019.02.047.

[42] Y. Hong, C. Zhou, Y. Zheng, L. Zhang, J. Zheng, X. Chen, B. An, Formation of strain-induced martensite in selective laser melting austenitic stainless steel, Mater. Sci. Eng. A 740–741 (2019) 420–426, https://doi.org/10.1016/j.msea.2018.10.121.

[43] S. Dépinoy, M. Sennour, L. Ferhat, C. Colin, Experimental determination of solute redistribution behavior during solidification of additively manufactured 316l, Scr. Mater. 194 (2021), 113663, https://doi.org/10.1016/j.scriptamat.2020.113663.

[44] K.M. Bertsch, Origin of dislocation structures in an additively manufactured austenitic stainless steel 316l, Acta Mater. 15 (2020).

[45] A.J. Birnbaum, J.C. Steuben, E.J. Barrick, A.P. Iliopoulos, J.G. Michopoulos, Intrinsic strain aging, Σ3 boundaries, and origins of cellular substructure in additively manufactured 316l, Addit. Manuf. 29 (2019), 100784, https://doi.org/10.1016/j.addma.2019.100784.

[46] V. Cruz, Q. Chao, N. Birbilis, D. Fabijanic, P. Hodgson, S. Thomas, Electrochemical studies on the effect of residual stress on the corrosion of 316l manufactured by selective laser melting, Corros. Sci. 164 (2020), 108314, https://doi.org/10.1016/j.corsci.2019.108314.

[47] T. Ronneberg, C.M. Davies, P.A. Hooper, Revealing relationships between porosity, microstructure and mechanical properties of laser powder bed fusion 316l stainless steel through heat treatment, Mater. Des. 189 (2020), 108481, https://doi.org/10.1016/j.matdes.2020.108481.

[48] O. Salman, C. Gammer, A. Chaubey, J. Eckert, S. Scudino, Effect of heat treatment on microstructure and mechanical properties of 316l steel synthesized by selective laser melting, Mater. Sci. Eng. A 748 (2019) 205–212, https://doi.org/10.1016/j.msea.2019.01.110.

[49] E. Tascioglu, Y. Karabulut, Y. Kaynak, Influence of heat treatment temperature on the microstructural, mechanical, and wear behavior of 316l stainless steel fabricated by laser powder bed additive manufacturing, Int. J. Adv. Manuf. Technol. 107 (5) (2020) 1947–1956, https://doi.org/10.1007/s00170-020-04972-0.

[50] X. Yang, F. Tang, X. Hao, Z. Li, Oxide evolution during the solidification of 316l stainless steel from additive manufacturing powders with different oxygen contents, Metall. Mater. Trans. B Process Metall. Mater. Process. Sci. 52 (4) (2021) 2253–2262, https://doi.org/10.1007/s11663-021-02191-w.

[51] F.C. Pinto, Recrystallization in non-conventional microstructures of 316l stainless steel produced by laser powder-bed fusion: effect of particle coarsening kinetics, J. Mater. Sci. 23 (2022).

[52] L. Cui, F. Jiang, R.L. Peng, R.T. Mousavian, Z. Yang, J. Moverare, Dependence of microstructures on fatigue performance of polycrystals: a comparative study of conventional and additively manufactured 316l stainless steel, Int. J. Plast. 149 (2022), 103172, https://doi.org/10.1016/j.ijplas.2021.103172.

[53] A. Smith, The diffusion of chromium in type 316 stainless steel, Metal Sci. 9 (1975) 375–378.

[54] D.S. Popkova, I.M. Ruslanov, A.Y. Zhilyakov, S.V. Belikov, The effect of the selective laser melting mode on second phases precipitation in 316l steel during subsequent heat treatment, IOP Conf. Ser.: Mater. Sci. Eng. 1029 (1) (2021), 012053, https://doi.org/10.1088/1757-899X/1029/1/012053.

[55] R.L. Plaut, C. Herrera, D.M. Escriba, P.R. Rios, A.F. Padilha, A short review on wrought austenitic stainless steels at high temperatures: processing, microstructure, properties and performance, Mater. Res. 10 (4) (2007) 453–460, https://doi.org/10.1590/S1516-14392007000400021.

[56] J. Sopousek, J. Vrestal, Phase equilibrium in the fe-cr-ni and fe-cr-c systems, Int. J. Mater. Res. 85 (1994), https://doi.org/10.1515/ijmr-1994-850209.

[57] K. Saeidi, F. Akhtar, Subgrain-controlled grain growth in the laser-melted 316 l promoting strength at high temperatures, R. Soc. Open Sci. 5 (5) (2018), 172394, https://doi.org/10.1098/rsos.172394.

[58] C.-C. Hsieh, W. Wu, Overview of intermetallic sigma phase precipitation in stainless steels, ISRN Metall. 2012 (2012) 1–16, https://doi.org/10.5402/2012/732471.

[59] W. Chen, T. Voisin, Y. Zhang, J.-B. Forien, C.M. Spadaccini, D.L. McDowell, T. Zhu, Y.M. Wang, Microscale residual stresses in additively manufactured stainless steel, Nat. Commun. 10 (1) (2019) 4338, https://doi.org/10.1038/s41467-019-12265-8.

[60] C. Parrens, J. Lacaze, B. Malard, J.-L. Dupain, D. Poquillon, Isothermal and cyclic aging of 310s austenitic stainless steel, Metall. Mat. Trans. A 48 (6) (2017) 2834–2843, https://doi.org/10.1007/s11661-017-4073-2.

[61] Y. Liu, Y. Yang, D. Wang, A study on the residual stress during selective laser melting (slm) of metallic powder, Int. J. Adv. Manuf. Technol. 87 (1–4) (2016) 647–656, https://doi.org/10.1007/s00170-016-8466-y.

[62] H. Yin, M. Song, P. Deng, L. Li, B.C. Prorok, X. Lou, Thermal stability and microstructural evolution of additively manufactured 316l stainless steel by laser powder bed fusion at 500–800 °C, Addit. Manuf. 41 (2021), 101981, https://doi.org/10.1016/j.addma.2021.101981.

[63] S. Gorsse, C. Hutchinson, M. Gouné, R. Banerjee, Additive manufacturing of metals: a brief review of the characteristic microstructures and properties of steels, ti-6al-4v and high-entropy alloys, Sci. Technol. Adv. Mater. 18 (1) (2017) 584–610, https://doi.org/10.1080/14686996.2017.1361305.

[64] A. Baldan, Review progress in ostwald ripening theories and their applications to nickel-base superalloys, J. Mater. Sci. 37 (2002) 2171–2202.

[65] Z. Zhu, W. Li, Q.B. Nguyen, X. An, W. Lu, Z. Li, F.L. Ng, S.M. Ling Nai, J. Wei, Enhanced strength–ductility synergy and transformation-induced plasticity of the selective laser melting fabricated 304l stainless steel, Addit. Manuf. 35 (2020), 101300, https://doi.org/10.1016/j.addma.2020.101300.

[66] Z. Zhu, Q. Nguyen, F. Ng, X. An, X. Liao, P. Liaw, S. Nai, J. Wei, Hierarchical microstructure and strengthening mechanisms of a cocrfenimn high entropy alloy additively manufactured by selective laser melting, Scr. Mater. 154 (2018) 20–24, https://doi.org/10.1016/j.scriptamat.2018.05.015.